JGR Atmospheres

RESEARCH ARTICLE
10.1029/2019JD032097

Special Section:
The Chinese Academy of Sciences Climate and Earth System Models (CAS-FGOALS and CAS-ESM) and Applications

Simulating and Evaluating Global Aerosol Distributions With the Online Aerosol-Coupled CAS-FGOALS Model

Hao Wang[1,2,3], Tie Dai[1,2], Daisuke Goto[4], Qing Bao[1], Bian He[1], Yimin Liu[1], Toshihiko Takemura[5], Teruyuki Nakajima[6], and Guangyu Shi[1,2,3]

[1]State Key Laboratory of Numerical Modeling for Atmospheric Sciences and Geophysical Fluid Dynamics, Institute of Atmospheric Physics, Chinese Academy of Sciences, Beijing, China, [2]Collaborative Innovation Center on Forecast and Evaluation of Meteorological Disasters/Key Laboratory of Meteorological Disaster of Ministry of Education, Nanjing University of Information Science and Technology, Nanjing, China, [3]College of Earth and Planetary Sciences, University of Chinese Academy of Sciences, Beijing, China, [4]National Institute for Environmental Studies, Tsukuba, Japan, [5]Research Institute for Applied Mechanics, Kyushu University, Fukuoka, Japan, [6]Earth Observation Research Center, Japan Aerospace Exploration Agency, Tsukuba, Japan

Abstract We implement an existing aerosol module named Spectral Radiation Transport Model for Aerosol Species (SPRINTARS) in the Chinese Academy of Sciences Flexible Global Ocean–Atmosphere–Land System (CAS-FGOALS) model and simulate the global aerosol properties over 2002–2014. The simulated surface mass concentrations of individual aerosols generally reproduce the observed ones. The simulated spatial-temporal distributions of the aerosol optical depths (AODs) are evaluated with multisource satellite retrievals, and the simulated AOD, Ångström Exponent (AE), and single scattering albedo (SSA) are further evaluated with the ground-based Aerosol Robotic Network (AERONET) measurements. The spatial distribution of the modeled AOD is found to be generally comparable to the satellite retrievals. The interannual and seasonal variations of the modeled AOD over various aerosol regimes are also overall consistent with the AERONET observations. With respect to the AE, our model can reproduce the interannual variations fairly well over the dust dominant regions, and generally capture the seasonal variations over the industrial domain regions. Over the industrial domain regions, however, the systematic underestimation of the simulated AE is found, which is in part due to the biases of wind fields and overestimation of the relative humidity (RH) by the host model. With respect to the SSA, our model can also generally reproduce the observed seasonal variations, while the modeled values are typically lower than the observations, especially over North Africa.

Key Points:

- The interannual and seasonal variation of modeled aerosol optical properties are overall consistent with the observations at most regions
- Biases of the meteorological fields are responsible for underestimation of the Ångström Exponent over the industrial dominant regions
- The seasonal variations of aerosol optical depth in the dust dominant region can be better reproduced with more realistic wind fields

Supporting Information:

- Supporting Information S1

Correspondence to:
T. Dai,
daitie@mail.iap.ac.cn

Citation:
Wang, H., Dai, T., Goto, D., Bao, Q., He, B., Liu, Y., et al. (2020). Simulating and evaluating global aerosol distributions with the online aerosol-coupled CAS-FGOALS model. *Journal of Geophysical Research: Atmospheres*, *125*, e2019JD032097. https://doi.org/10.1029/2019JD032097

Received 24 NOV 2019
Accepted 25 NOV 2020

1. Introduction

Aerosols have great effects on the Earth's radiation budget by scattering and absorbing solar radiation, as well as complexly affecting the microphysical properties and lifetime of clouds, and hence impact the Earth's climate and hydrological cycle (Chylek & Wong, 1995; Ramanathan et al., 2001; Twomey, 1974, 1991). Despite numerous aerosol studies, currently, the aerosol particles influencing radiative forcing, especially aerosol-cloud interaction, are still one of the largest uncertainties in model simulations for global climate projection (Boucher et al., 2013; Haywood & Boucher, 2000; Myhre, Shindell, et al., 2013). One of the key factors resulting in such large uncertainty in model radiative forcing and its climatic effect can be attributed to the diversity in aerosol optical properties and their spatial-temporal distributions (Myhre, Samset, et al., 2013).

In the past decades, information about the aerosol optical properties were obtained from various evolving aerosol observing systems, including ground-based global networks such as the AERONET (AErosol RObotic NETwork; Holben et al., 1998) and CARSNET (China Aerosol Robot Sunphotometer NETwork; Che et al., 2009), and space-based remote sensing platforms such as MODIS (Moderate Resolution Imaging Spectroradiometer; Remer et al., 2005), MISR (the Multi-angle Imaging SpectroRadiometer; Martonchik et al., 1998), AHI (Advanced Himawari Imager; Bessho et al., 2016), CALIPSO (the Cloud-Aerosol Lidar and Infrared Pathfinder Satellite; Winker et al., 2013), AATSR (Advanced Along-Track Scanning Radiometer; Bevan et al., 2012), SeaWiFS (Sea-viewing Wide Field-of-view Sensor; Hsu et al., 2019), VIIRS (Visible Infrared Imaging Radiometer; Hsu et al., 2019), and POLDER (Polarization and Directionality of Earth's Reflectance; Dubovik et al., 2011; 2014). The highly accurate ground-based observations of aerosols could be used

to evaluate satellite retrievals, while remote sensing can overcome the limitations of spatial coverage of these ground measurements with various spatial-temporal resolutions (Kittaka et al., 2011; Remer et al., 2005). Despite this continuous progress, however, large diversities still remain among various satellite observations (Ma et al., 2013), including limited understanding of the global aerosols distribution. The aerosol products of AATSR Dual View (ADV) and SeaWiFS showed relatively lower spatial coverage with numerous missing values over MODIS products, which cover most areas (average of 87%) of the world (Wei et al., 2019). The satellite data sets showed varying levels of consistency, depending on the region (Holzer-Popp et al., 2013; Nabat et al., 2013), with the largest discrepancies seen in regions with persistent heavy cloud cover (Sayer et al., 2018).

Due to a lack of knowledge about the accurate spatial and temporal distributions of aerosol optical properties, global aerosol transport models, which are coupled with the general circulation model or chemical transport model (CTM), have emerged as important tools for filling in these observational gaps to simulate aerosol optical properties, such as aerosol optical depth (AOD), Ångström exponent (AE), and single scattering albedo (SSA), for radiative forcing estimation. To date, however, different models still show a large diversity of global aerosol distribution (Cesnulyte et al., 2014; Dai et al., 2015; Ma & Yu, 2015; Pozzer et al., 2015; Sheel et al., 2018). An important way in which to reduce this diversity is by observation and evaluation of the model performances with respect to the aerosol optical properties, which can lead to model improvements in the aerosol size distribution, hygroscopic growth, refractive indices, mixing state, emissions, and other aspects to better quantify the spatial and temporal distribution of aerosols and study their global climatic effects (Chin et al., 2009; Lamarque et al., 2012; Liu et al., 2016; Ma & Yu, 2015; Mann et al., 2014; Seinfeld & Pandis, 2006; Tsigaridis et al., 2014).

The Chinese Academy of Sciences (CAS) Flexible Global Ocean–Atmosphere–Land System (FGOALS-f3-L) model developed by the State Key Laboratory of Numerical Modeling for Atmospheric Sciences and Geophysical Fluid Dynamics (LASG), Institute of Atmospheric Physics (IAP), CAS (Bao et al., 2019; He et al., 2019; J. Li et al., 2019), has continuously contributed to the Coupled Model Intercomparison Project (CMIP) from the initial phase to the current phase of the CMIP6, and to the assessment reports of the Intergovernmental Panel on Climate Change (IPCC; Zhou et al., 2015). A significant advantage of FGOALS-f3-L is that a higher resolution simulation (~25 km) can be performed with the updated dynamical core using a finite volume on the cubed-sphere grid (S. J. Lin, 2004; Putman & Lin, 2007). To date, however, CAS-FGOALS-f3-L only reproduces the direct aerosols radiation effect offline and lacks the interactions between aerosols and cloud. The prescribed aerosols are taken from the National Center for Atmospheric Research (NCAR) CAM-Chem model (Lamarque et al., 2012), which are unable to match the meteorological fields of the model for every time step and hampers the study of the climate effects, such as assessing the effective radiative forcing of anthropogenic aerosols.

In this study, we implement an existing aerosol module named Spectral Radiation Transport Model for Aerosol Species (SPRINTARS; Takemura et al., 2005) in the CAS-FGOALS-f3-L model. An important feature of the new version is that of replacing the offline aerosol with the online aerosol model and adding the interaction between aerosol and cloud. The main objective of this study is to evaluate the performance of the new coupled aerosol model with multiple platform observations. We simulate the global aerosol distributions over the 2002–2014 period. The simulated surface mass concentrations of each aerosol species are evaluated with in situ observations, and the simulated aerosol optical properties are evaluated with satellite-based MODIS, MISR, AATSR-SU, and SeaWiFS and surface-based AERONET observations.

This study is organized as follows. In Section 2, we describe the newly developed aerosol online coupled model and observations used for evaluation. In Section 3, the performances of the simulated aerosols are evaluated with comparisons between the surface mass concentration observations, the MODIS, MISR, AATSR-SU, and SeaWiFS as well as the AERONET observations. In Section 4, we discuss the overall model results. The brief conclusions are given in Section 5.

2. Model and Observations

2.1. Model Description

CAS FGOALS-f3-L is the latest-generation global climate model (GCM), which is developed by the LASG, IAP, and CAS. Replaced with the former Spectral Atmosphere Model (SAMIL; Bao et al., 2010, 2013; Wu

Table 1
Summary of the Emission Source, Species, and Mass Ratio of OC and BC for Carbonaceous Aerosols

Emission source	Species	OC/BC mass ratio
ANTBC (50%)	BC	Pure BC
Terpene	SOC	Pure SOC
BBOC	OC/BC (1)	8.28
BBBC	OC/BC (2)	6.92
ANTBC (50%)	OC/BC (3)	3.33
ANTOC	OC/BC (4)	5.64

Abbreviations: ANTBC: anthropogenic black carbon source, terpene: secondary organic carbon (SOC) from the gas-to-particle conversion of the terpenes emitted from vegetation, ANTOC: anthropogenic organic carbon source; BBBC: biomass burning black carbon source; BBOC: biomass burning organic carbon source.

et al., 1996), version 2 of the Finite-volume Atmospheric Model (FAMIL2; Bao et al., 2019; He et al., 2019; J. Li et al., 2019; Zhou et al., 2015), as the latest generation the atmospheric component, it is used in the atmospheric model of LASG. The dynamical core of FAMIL2 uses a finite volume on a cubed-sphere grid (S. J. Lin, 2004; Putman & Lin, 2007) that covers the globe with six tiles; each tile can contain a minimum of number of grid cells (C48, about 200 km) to a maximum of number of grid cells (C1536, about 6.25 km) (J. X. Li et al., 2017; Zhou et al., 2012). Compared with the previous spectral longitude-latitude grid (Bao et al., 2013), the unique design of the cubed-sphere grid of FAMIL2 resulted in a higher resolution simulation to be performed. Hybrid coordinates over 32 layers are used in the model, which extend from the surface to 1 hPa. A new turbulence parameterization scheme with a nonlocal high-order closure (Bretherton & Park, 2009) replaced the previous "nonlocal" first-order closure scheme. The single-moment microphysical parameterization used in FAMIL2 can explicitly treat the mass mixing ratio of six hydrometeor species (water vapor, cloud water, cloud ice, rain, snow, and graupel) (Harris & Lin, 2014; Y. L. Lin et al., 1983; Zhou et al., 2019). More precise cloud fractions can be diagnosed by the scheme of diagnosing the cloud fractions, which consider both relative humidity (RH) and cloud mixing ratio (Xu & Randall, 1996) as used in FAMIL2. A convection-resolving precipitation parameterization (Bao et al., 2019) is used in FAMIL2, which can calculate the microphysical processes in the cumulous scheme for both deep and shallow convection explicitly. In addition, a new radiation transfer scheme Rapid Radiative Transfer Model for GCMs (RRTMG), which used the correlated-k approach (Clough et al., 2005) to calculate the irradiance and heating rates are introduced into FAMIL2. The land and sea ice models adopt version 4.0 of the Community Land Model (CLM4; Oleson et al., 2010) and version 4 of the Los Alamos sea ice model (CICE4; Hunke & Lipscomb, 2010), respectively. The coupled module used the version 7 coupler (CPL7) from the NCAR (http://www.cesm.ucar.edu/models/cesm1.0/cpl7/) to exchange the flux among these components.

The aerosol module called SPRINTARS (Goto et al., 2011; Takemura et al., 2000, 2002, 2005, 2009) has been online coupled with the FAMIL2 in this study. A single-moment scheme is used to calculate the mass mixing ratios of the main tropospheric aerosol components (soil dust, sea salt, sulfate, and carbonaceous aerosols) and the precursor gases of sulfate. The main aerosol processes are treated, including emission, advection, convection, diffusion, sulfur chemistry, dry deposition, wet deposition, and gravitational settling.

In SPRINTARS, the soil dust particles are divided by radius into 10 bins from 0.1 to 10 μm. The emission mass flux F is calculated at each model time step with the parameterization scheme as follows (Dai et al., 2018; Takemura et al., 2000):

$$F = f(r)C\left(\frac{W_{gt} - W_g}{W_{gt}}\right)\left(|\upsilon_{10}| - u_t\right)|\upsilon_{10}|^2 \cdot 10^{-9} \quad (1)$$

where $|\upsilon_{10}|$ is the surface wind speed at a 10 m height, W_g is the soil moisture, $f(r)$ is the normalized emission intensity related to the dust effective radius r, C is the coefficient depending on the different dust source areas (Figure 1c and Table 1 in Dai et al., 2018), W_{gt} is the threshold soil moisture depending on the region, and u_t is the threshold set to 6.5 ms^{-1}. The sea salt particles are divided by radius into four bins from 0.1 to 10 μm (Takemura et al., 2009). The emission flux F, which is a function of the wind speed at a 10 m height and the particle radius based on Monahan et al. (1986), is calculated at every model time step.

The emission sources of carbonaceous aerosols are divided into five categories in the model as follows: anthropogenic black carbon source (ANTBC), biomass burning black carbon source (BBBC), anthropogenic organic carbon source (ANTOC), biomass burning organic carbon source (BBOC), and the gas-to-particle conversion of terpene. The first four emission inventories are all from the Community Emissions Data System (CEDS; Hoesly et al., 2018; van Marle et al., 2017) for CMIP6 (https://esgf-node.llnl.gov/search/input4mips/). The terpene emissions data is from the MEGANv2.10 biogenic emission inventories (https://

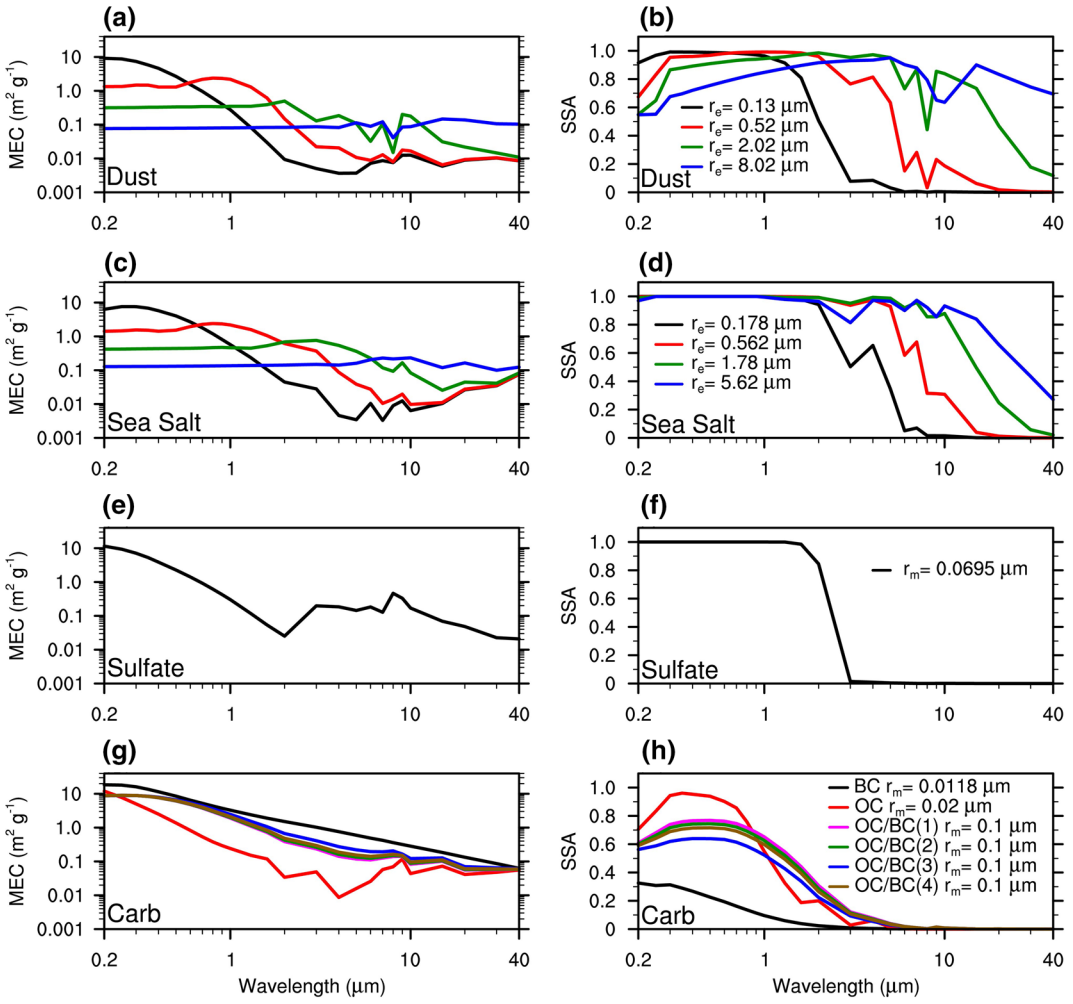

Figure 1. (a, c, e, and g) The spectra of the mass extinction coefficient (MEC) and (b, d, f, and h) single scattering albedo (SSA) of each species for the dry particle aerosols.

eccad3.sedoo.fr/). In SPRINTARS, two factors with values of 1.6 and 2.6 for ANTOC and BBOC are applied for the conversion of organic carbon into organic matter (Malm et al., 1994, 2003), respectively. The internal mixtures of BC and OC (OC/BC) are considered (Takemura et al., 2009). The mass ratio of OC and BC for each source in the model is listed in Table 1, following Takemura et al. (2002). A 50% mass of ANTBC is considered as an external mixture (i.e., pure BC), and pure OC is produced from the terpenes using a 5% yield rate (Liousse et al., 1996). The particle size distributions of carbonaceous aerosols (BC, OC, and OC/BC) are assumed to be monomodally lognormal size distributions with dry modal radii of 0.0118, 0.02, and 0.1 μm, respectively, while the geometric standard deviations are 2.0, 1.8, and 1.562, respectively. These assumptions are the same as those in Dai et al. (2014).

The precursor gases of sulfate aerosols are from the three following categories: dimethylsulfide (DMS), anthropogenic sulfur dioxide source ($ANTSO_2$), and biomass burning sulfur dioxide source ($BBSO_2$). The emission flux of DMS from oceanic phytoplankton is parameterized as a function of the downward surface solar flux (Takemura et al., 2000). The emissions inventories of $ANTSO_2$ and $BBSO_2$ are all from the CEDS for CMIP6. For SPRINTARS, the sulfur chemistry has been described in detail by Takemura et al. (2000). Briefly, DMS is oxidized by OH radicals to form SO_2 and sulfate in the gas phase, and SO_2 mainly reacts with OH radicals in the gas phase and H_2O_2 and O_3 in the liquid phase, which are calculated using three-dimensional monthly oxide fields of three free radicals (OH, O_3, and H_2O_2) prescribed from CHASER, a global CTM (Sudo et al., 2002). The particle size distribution of the sulfate follows that of Dai et al. (2014), using

a monomodally lognormal size distribution with dry modal radii of 0.0695 μm and geometric standard deviations of 1.526.

The aerosol densities and refractive indices of all aerosols are the same as those used by Takemura et al. (2002) and Dai et al. (2014). Meanwhile, except for the hydrophobic aerosols of dust and pure BC, the hygroscopic aerosols of the sea salt, sulfate, OC, and OC/BC are parameterized as a function of RH (Takemura et al., 2002, Table 4), and the mass extinction coefficient and absorption coefficient are calculated at eight RH using the Mie scattering algorithm (Dai et al., 2014). The simulated optical properties can be calculated with the precalculated optical parameters and simulated mass concentration of each species. AOD represents the aerosol extinction capacity in the atmospheric column and is derived as the mass extinction coefficient multiplied by the aerosol mass. AE represents the spectral change in AOD and characterizes the size of the aerosol particles and is calculated according to $-\log\left(\tau_{870\mathrm{nm}} / \tau_{440\mathrm{nm}}\right) / \log\left(\lambda_{870\mathrm{nm}} / \lambda_{440\mathrm{nm}}\right)$, where τ and λ represent AOD and wavelengths, respectively. SSA represents the aerosol scatter capacity and is calculated as the ratio of the scattering optical depth and extinction optical depth.

Figure 1 shows the spectra of the mass extinction coefficient and single-scattering albedo of each species for the dry particle aerosols used in the model. Generally, the mass extinction coefficient of the fine mode aerosols (e.g., sulfate and carbonaceous aerosols) at short wavelengths (0.2–12.2 μm in the model with RRTMG radiation transfer scheme) decreases as the wavelength increases, whereas the mass extinction coefficient of the coarse mode aerosols (e.g., dust and sea salt aerosols) at short wavelengths does not change with the wavelength, which implies a much lower AE for dust and sea salt than sulfate and carbonaceous aerosols. The single-scattering albedos of sea salt and sulfate almost reach 1, indicating that their absorptions are quite weak and negligible. In addition, a weak absorption for dust aerosols and a strong absorption for BC aerosols are found. The internal mixture of carbonaceous aerosols also reveals a stronger absorption than that of OC but weaker absorption than that of BC.

For the interaction of aerosol and cloud, the aerosol number concentration can be calculated by predicted aerosol mass mixing ratios, pre-prescribed particle size (dry mode radius and standard deviations), and particle density in each model time step in SPRINTARS. The activation scheme named ARG (Abdul-Razzak & Ghan, 2000; Takemura et al., 2005), considering particle size, aerosol chemical component, and updraft velocity, is used in the model for water stratus clouds. The berry-type autoconversion scheme (Berry, 1968) is adopted in the model, which includes a cloud condensation nuclei (CCN) effect and its formula is the same as that used by Sato et al. (2018).

2.2. Observations Data Set

2.2.1. AERONET

AERONET is a global ground-based Sun photometer network deployed for measurement of aerosol optical properties with high spectral-temporal resolutions (Holben et al., 1998). The network imposes standardization of instruments, calibration, processing, and distribution. Due to the uncertainty of AERONET AOD at Level 2.0 (quality assured) being ~0.01–0.02 (Smirnov et al., 2000), it can serve as a truth value to assess AOD and validate satellite-retrieved AOD. In addition, it is noticed that the uncertainty of AERONET SSA can increase significantly in low AOD situations due to the limitation of instrument sensitivity. The AERONET SSA has an uncertainty of 0.03 when AOD (440 nm) is great than 0.2 and 0.05 to 0.07 when AOD (440 nm) is less than 0.2 (Dubovik et al., 2000). In the present study, we use the cloud-screened and quality-assured AERONET Level 2.0 daily average data (https://aeronet.gsfc.nasa.gov/cgi-bin/combined_data_access_inv) for comparison. As not all the sites have large temporal coverage, we choose those sites with more than 5 days' observations every month and at least 12-month data available over the period of 2002–2014 for our analysis; we further eliminate the sites with a low spatial domain (<300 km) according to the site assessment from Kinne et al. (2013). The AOD and SSA at 550 nm obtained by spectral interpolation at both 440 and 675 nm are used under the assumption that they are proportional to the wavelength on a logarithmic scale (Dai et al., 2014). The AE calculated from AODs at 440 and 870 nm is used. Finally, the simulated values of aerosol optical properties (AOD, AE, and SSA) are sampled consistently with AERONET site measurements for comparison.

2.2.2. MODIS, MISR, AATSR-SU, and SeaWiFS

The MODIS is a key instrument aboard the Terra and Aqua satellites (Salomonson et al., 1989). It views the entire Earth's surface every 1–2 days with a swath of 2,330 km, acquiring data in 36-spectral bands (0.41–14.4 μm), and is a well-calibrated spectroradiometer with spatial resolutions of 250, 500, and 1,000 m (Levy et al., 2010; Remer et al., 2008). After continuous validations and evaluations, one MODIS AOD product retrieved by a dark target (DT) algorithm, which has limitations over bright surfaces in visible channels, has clear expected errors (EEs): [±(0.05 + 0.15 AOD)] over land and [+(0.04 + 0.10 AOD), −(0.02 + 0.10 AOD), asymmetric] over ocean (Levy et al., 2013). Another MODIS AOD product which can be better retrieved from desert surfaces by a deep blue (DB) algorithm is applied only over land, and its EEs are ∼[± (0.03 + 0.21 AOD)] for "arid" and [± (0.03 + 0.18 AOD)] for "vegetated" path (Hsu et al., 2013). The MODIS Level 3 AOD product is created by aggregating the MODIS Level 2 AOD product that considers only the best cloud-free pixels as a preprocessing step (Martins et al., 2002; Remer et al., 2005). In the present study, the daily MODIS Collection 6.1 Level 3 AODs combined with the DT and DB algorithms (variable name "AOD_550_Dark_Target_Deep_Blue_Combined_Mean") at a 1 × 1° resolution from both the Terra and Aqua satellites are used, which can be considered as a "best-of" AOD product that combines DB, DT-land, and DT-ocean based on a simple merge for increasing the spatial coverage (Levy et al., 2013). The Terra AODs are available since early 2000, whereas the Aqua AODs are available since mid-2002. In order to make full use of these data, we average the available MODIS L3 AOD retrievals from both Terra and Aqua over the period 2002–2014 for our analysis.

The MISR (Martonchik et al., 1998) is one of the first multiangle, multispectral space-based imagers on the Terra satellite, which is designed to improve our understanding of the fate of sunlight in the Earth's environment. It has an assembly of nine cameras with four spectral channels (blue, green, red, and near-infrared) at nine different viewing angles, swathing about 380 km. The observation with a well-calibrated and georectified multiangular imagery enables the generation of long-term data records, including aerosol properties over land and ocean. Recently, a new method is introduced to improve the retrieving AOD over dark water and screen high-AOD retrieval blunders through the use of thresholds on different cost functions (Witek et al., 2018). In this study, the latest MISR Version 23 monthly globally gridded aerosol mean AOD at 555 nm (green band) in 0.5 × 0.5° resolution over the period 2002–2014 is used for comparison.

The AATSR aboard on ENVISAT is used to observe the Earth by dual-view, which is a part of Climate Change Initiative (CCI). The AOD retrieval algorithms of AATSR-SU is the Swansea algorithm (SU) by the University of Swansea (Xie et al., 2017), which employs a simple model to estimate the water-leaving radiance from the ocean at the red and infrared channels over the ocean. Over land, the SU algorithm estimates the surface spectral reflectance using the dual-view feature (Bevan et al., 2012; North, 2002). In our study, the latest Version 4.3 monthly AATSR-SU products in 1 × 1° resolution over the period 2002–2011 are used.

SeaWiFS is the first mission on ocean-colors in the United States and internationally, which can provide a long-term record of optical properties and ocean biology for climate research (Hooker & McClain, 2000). The multi-spectral radiometer of SeaWiFS can collect data over a wide swath with a resolution of ∼1 km (McClain et al., 2004). SeaWiFS is mainly for providing ocean color measurements, and it generates aerosol products using the DB algorithm (Wei et al., 2019). One of the advantages of SeaWiFS aerosol optical products is that the SeaWiFS can avoid specular reflection of the Sun on the ocean surface (Hooker & McClain, 2000). In our study, the SeaWiFS Version 4 monthly aerosol products with 1 × 1° resolution which are available over the period 2002–2010 are used.

2.2.3. Surface Mass Concentrations

Four freely available compilations of aerosol surface concentrations, which represent the present-day climatology of aerosol surface concentration observations, are used to evaluate the simulated aerosol surface concentrations. The first data set was managed by the Rosenstiel School of Marine and Atmospheric Science at the University of Miami, which are based partly on measurements taken during the sea/air exchange (SEAREX) program in 1979 (Prospero et al., 1989). Most measuring sites are located far downwind of dust emission sources. Here, we use dust and sea salt surface concentrations data covering the period of 1981–1998 for climatological comparison. The second data set is from the Interagency Monitoring of Protected Visual Environment (IMPROVE) database (http://views.cira.colostate.edu/fed/QueryWizard/

Default.aspx). IMPROVE is designated as the visibility monitoring network in the United States and was initially established as a national visibility network in 1985, which is mainly used for observation of aerosols, air quality, and optical parameters. We select sulfate, OC, and BC surface concentrations from 160 sites with more than 5 days of observation every month and at least 12 months' data available over the period 2002–2014 for comparison. The third data set is from the co-operative program for monitoring and evaluation of the long-range transmission of air pollutants in Europe (unofficially "European Monitoring and Evaluation Programme," EMEP). The data are subject to national quality assessment and can be downloaded freely from the website (https://projects.nilu.no//ccc/emepdata.html). Similar to IMPROVE data sample method, a total of 46 sites are selected for sulfate concentrations comparison and 6 sites for OC and BC concentrations comparison. The last data set is from 14 long-term observational stations within China and monthly mean mass concentration are collected during 2006 and 2007 (Zhang et al., 2012). After we eliminate the Xi'an site that is influenced a lot by local construction activity, the 13 sites, which measured mass concentrations of BC, OC, and sulfate in 2006, are selected for comparison.

3. Results

In order to evaluate the performance of this new coupled aerosol model with multiple-platform observations, an AMIP-like experiment is performed in this study. It is noted that the CMIP6 forcing data go until 2014, and most observational data can be obtained after the 20th century. Therefore, the period 2002–2014 is selected for simulation and comparison, despite missing out on all the observational data sets that have been assembled in recent years.

For quantitative comparison, model performances against the observations are measured by four statistical metrics: correlation coefficient (R), mean bias (B), root-mean-square error (E), and skill score (S). B is defined as the average difference between all model-observed pairs (Chin et al., 2009) and can be written as

$$B = \frac{1}{N}\sum_{i=1}^{N}\left(C_m - C_o\right) \tag{2}$$

where C_m is the simulated value, C_o is the observed value, and N is the total number of observations. E is a frequently good overall measure of the differences between all model-observed pairs and is defined as the following formula:

$$E = \sqrt{\frac{1}{N}\sum_{i=1}^{N}\left(C_m - C_o\right)^2} \tag{3}$$

The skill score S is a relatively comprehensive statistical index for the model evaluation, which relates to R and the standard deviation of the model and observed results. It is calculated as

$$S = \frac{4\left(1+R\right)}{\left(\sigma_f + \frac{1}{\sigma_f}\right)^2\left(1+R_0\right)} \tag{4}$$

where σ_f is the result of the standard deviation of model outputs divided by the standard deviation of observations, and R_0 is set to 1, which is the maximum of R (Chin et al., 2009; Taylor, 2001).

3.1. Aerosol Lifecycles

Figure 2 shows the spatial distribution of the annual average aerosol emission rates of dust, sea salt, BC, OC, and sulfur over the 2002–2014 period that are used in the model. It is obvious that the major dust sources are in the Sahara, the Middle East, and Asia deserts. The maximum sea salt emission exists in the mid-high latitude area, especially in the Southern Ocean, which has strong winds. Higher BC and OC emissions are found in East Asia, South Asia, South America, and South Africa. Sulfate aerosols can be produced by the chemical reaction of SO_2. A minor SO_2 source is from the DMS produced by

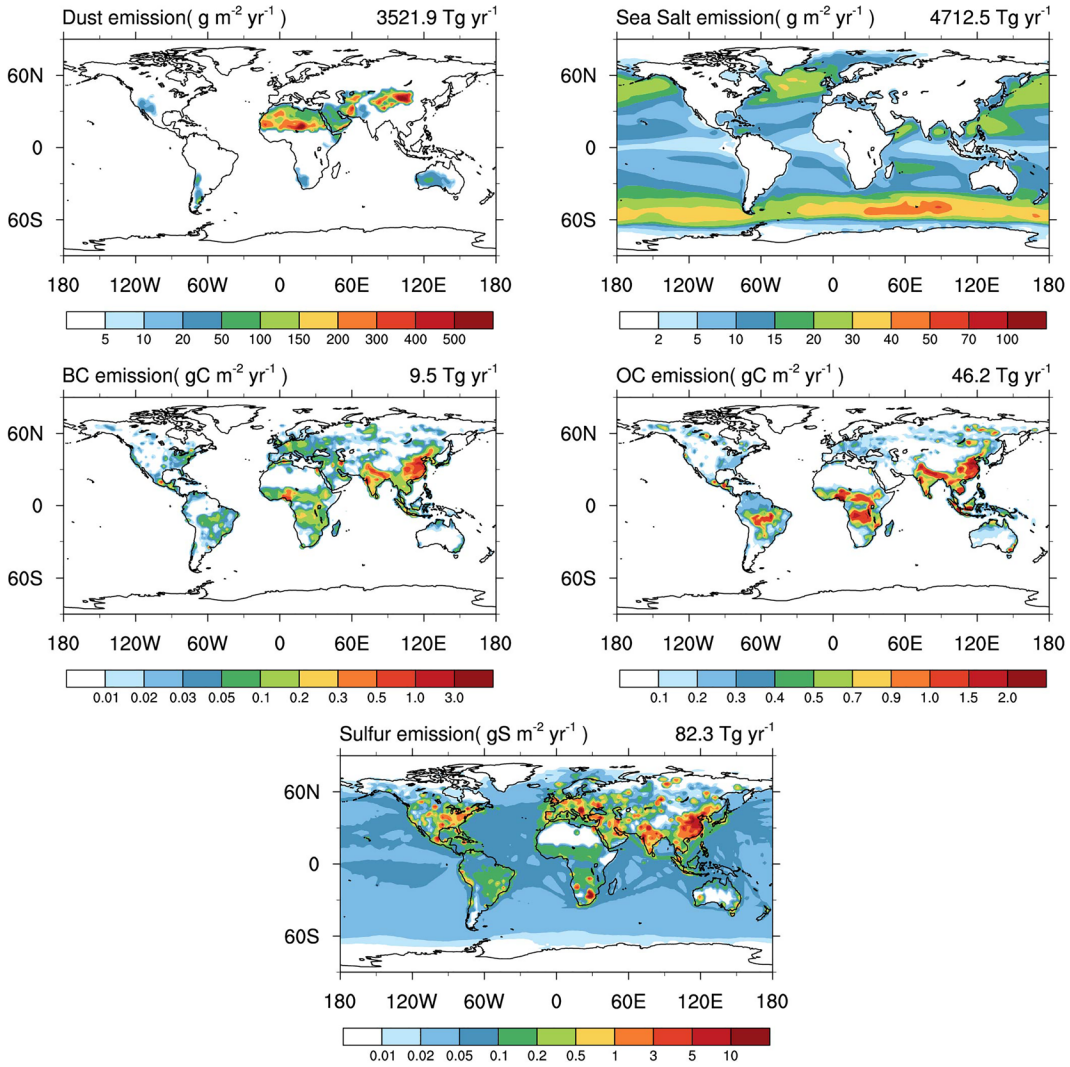

Figure 2. Annual average aerosol emission rates of dust, sea salt, BC, OC, and sulfur over the 2002–2014 period used in the model. The global annual average values are labeled at the top-right of each subplot.

phytoplankton in the ocean, and the major SO_2 sources in the East Asia, South Asia, Europe, North America, and South Africa are apparent and are usually associated with human activities and economic development.

Table 2 shows the global annual average aerosol emissions, burdens, lifetimes, and loss frequencies. The loss frequencies, namely, removal rate coefficients, are calculated as in Textor et al. (2006, Equation 7). The emission flux of natural aerosols (such as dust and sea salt) accounts for the largest emission flux of all aerosol species in the model. For the dust aerosols, a shorter dust lifetime (~2 days) is mainly induced by stronger dry deposition (dry deposition = turbulent dry deposition + sedimentation) in the model, especially turbulent dry deposition, as its removal rate is five times of that for sedimentation through further analysis. These results are similar to a previous study on SPRINTARS (Takemura et al., 2000, Figure 5), which implies that the lifetime of dust aerosol mainly depends on the dust emission scheme and deposition scheme. For sea salt aerosol, the shortest lifetime in the model is mainly due to strong wet deposition and dry deposition. In addition, black carbon, particles of organic matter, and sulfate are dominated by fine modes and wet removal processes.

Table 2
Global Annual Average Aerosol Emissions, Burdens, Lifetimes, and Loss Frequencies

Species	Emissions ($Tgyr^{-1}$)	Burden (Tg)	Lifetime (days)	k_{wet} ($days^{-1}$)	k_{dry} (day^{-1})
Dust	3521.90 ± 244.35	18.91 ± 1.47	1.96 ± 0.10	0.079 ± 0.004	0.719 ± 0.007
Sea salt	4712.47 ± 42.91	4.70 ± 0.03	0.36 ± 0.00	0.871 ± 0.006	2.187 ± 0.008
Black carbon	9.47 ± 0.62	0.18 ± 0.01	7.08 ± 0.13	0.111 ± 0.001	0.058 ± 0.001
POM	101.63 ± 4.55	1.34 ± 0.06	4.80 ± 0.11	0.176 ± 0.001	0.062 ± 0.002
Sulfate (S only)	41.54 ± 1.00	0.58 ± 0.02	5.12 ± 0.17	0.173 ± 0.000	0.045 ± 0.001

Note. For each cell, the top number is the multiyear mean (±standard deviation) result of the CAS FGOALS simulations for the 2002–2014 period, k_{wet} and k_{dry} representing wet and dry removal rate coefficients, both are calculated as in Textor et al. (2006, equation 7).

Abbreviation: POM, particles of organic matter.

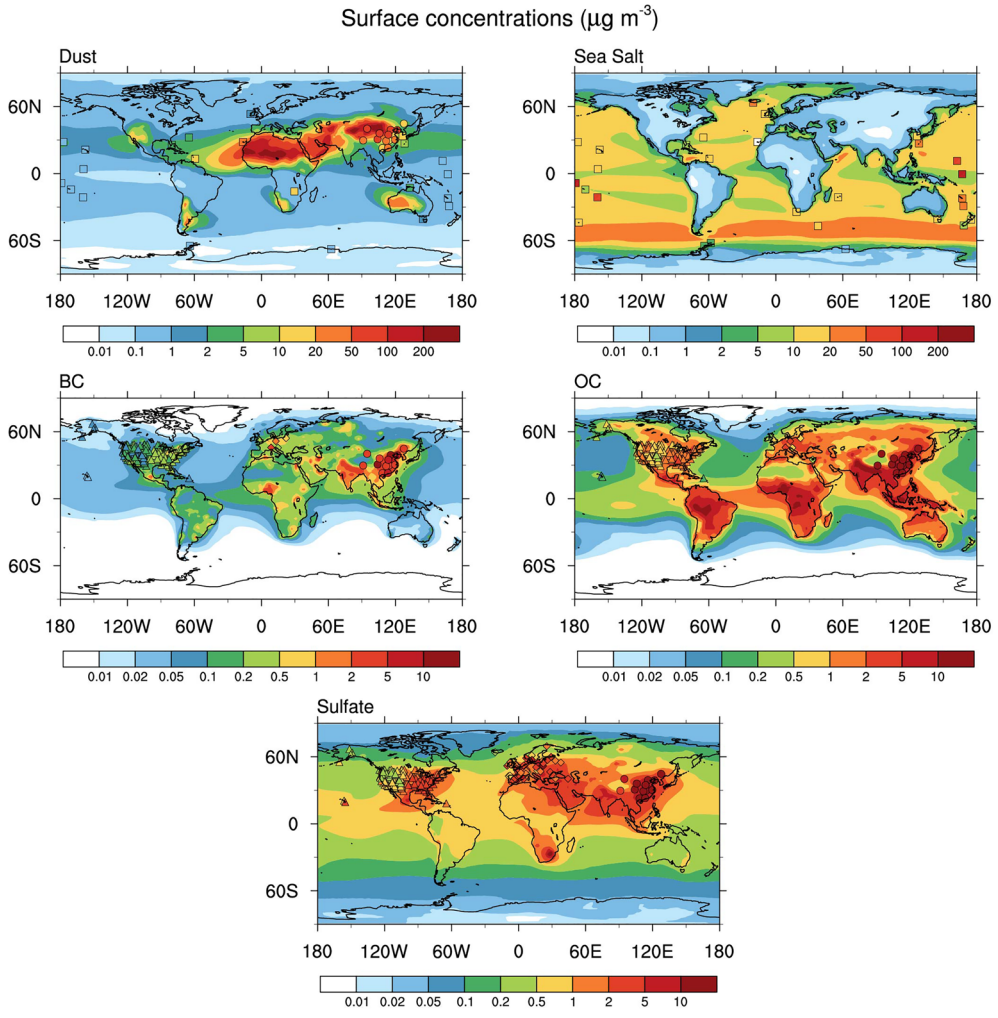

Figure 3. Annual average aerosol surface concentrations (μg m^{-3}) of dust, sea salt, BC, OC, and sulfate for the 2002–2014 period. Four symbols represent site observations from different sources: square = University of Miami sites (global); triangle = IMPROVE (America); circle = East Asia sites; and rhombus = EMEP (Europe). Both the simulated results and observations have the same color bar. EMEP, European Monitoring and Evaluation Programme; IMPROVE, Interagency Monitoring of Protected Visual Environment.

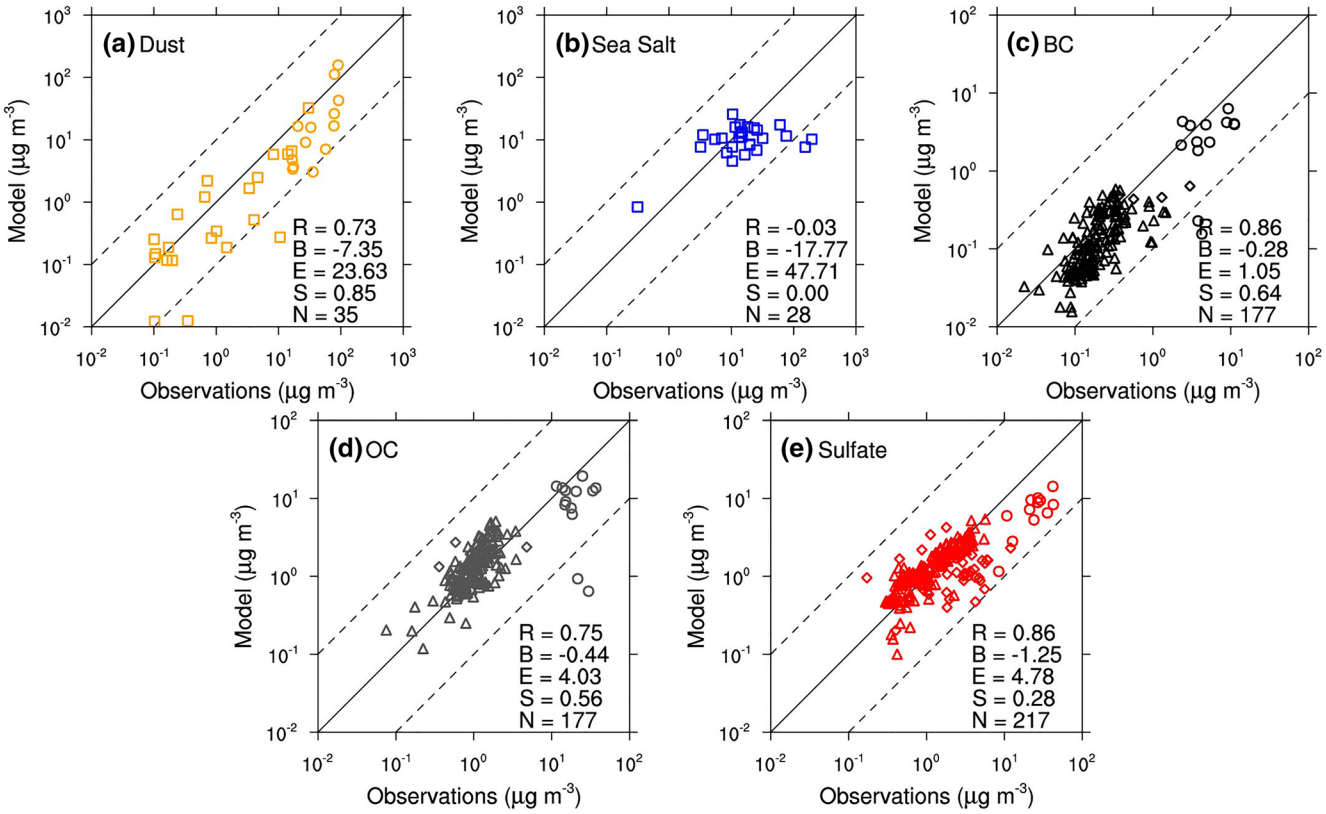

Figure 4. Scatterplot of modeled versus site-observed surface mass concentrations. (a) Dust, (b) Sea salt, (c) Black carbon (BC), (d) Organic carbon (OC), (e) Sulfate. The black continuous line is the 1:1 line, whereas the black dotted lines correspond to the 10:1 and 1:10 lines. The symbols representing the sites observations are the same as in Figure 3. R = correlation coefficient, B = absolute bias, E = Root mean square error, S = skill score, and N = total number of observation sites.

3.2. Aerosol Surface Mass Concentrations

Figure 3 shows the spatial distributions of the simulated annual average aerosol surface mass concentrations. The sites are marked with different symbols to represent different data sources. It is clear that the surface concentrations are closely related to the emission intensity of the aerosols or their precursors and are affected by atmospheric circulation. The maximum concentrations tend to occur in high-emission areas. Aerosol plumes can extend to the northeast corner of South America from North Africa (such as dust, BC, and OC) and the northwest Pacific from East Asia (such as dust, BC, OC, and sulfate). Figures 3 and 4 both show that the simulated aerosol surface concentrations have similar regional variability and magnitude with the observations. The modeled dust surface concentrations (Figure 4a) are well correlated with the observations ($R = 0.73$), suggesting that the model can reasonably characterize the dust surface distribution. According to reanalysis data, the noticeable low bias ($B = -7.35$) in dust concentration, partly due to the wind speed in 1980–1990s (dust concentration measurement period), is stronger than that in the period 2002–2014s (simulation period) in most land areas. The modeled sea salt surface concentrations (Figure 4b) are poorly correlated with the observations ($R = -0.03$) and have a significant low bias ($B = -17.77$), this is possibly in part due to the resolution in our model being too large (~200 km), which can smooth the extreme points. In addition, Fei et al. (2019) recently pointed out that large particle size sea salt (radius of the dry particle >10 μm) can account for ~28.5% of the total sea salt mass, so the neglect of large particle size sea salt may also lead to an underestimation of the sea salt mass concentration. According to comparisons of the simulated BC, OC, and sulfate aerosol surface concentrations with the site observations (Figures 4c–4e), the modeled results are well correlated with the surface observed concentrations for BC ($R = 0.86$), OC ($R = 0.75$), and sulfate ($R = 0.86$), with a slight low bias for BC ($B = -0.28$), OC ($B = -0.44$), and sulfate

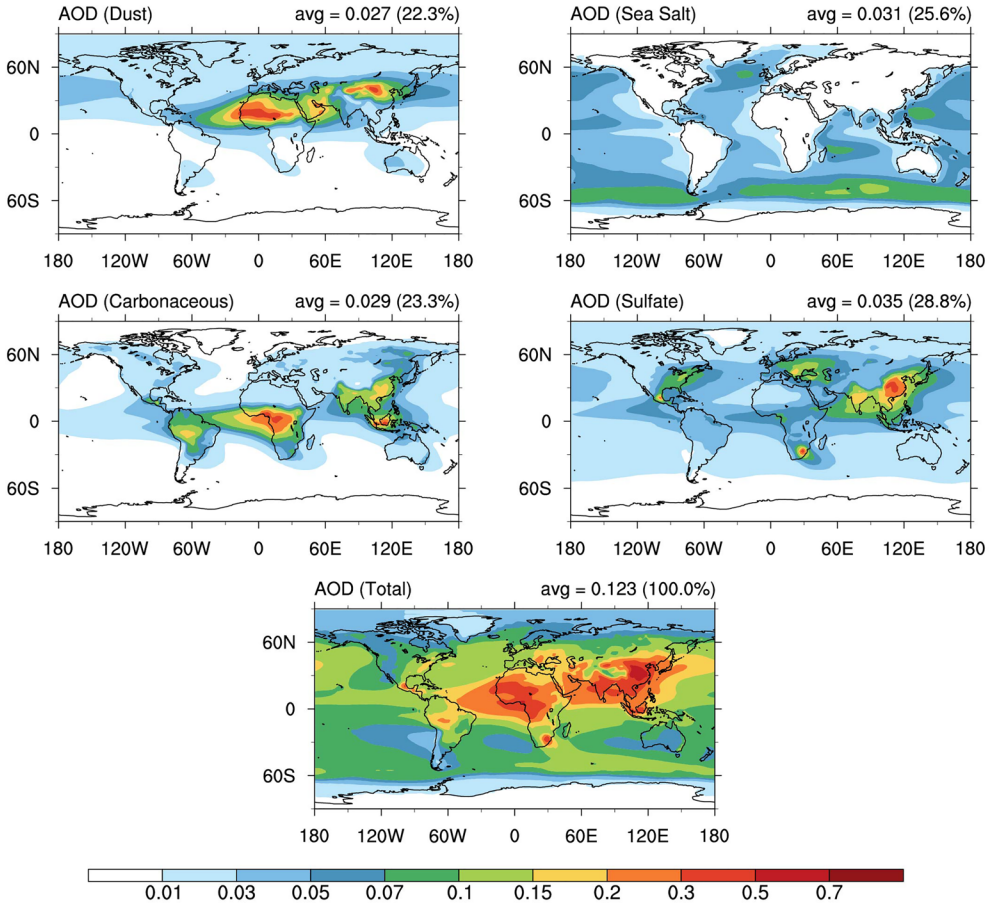

Figure 5. Annual average aerosol optical depth of dust, sea salt, carbonaceous, sulfate, and total aerosol during the 2002–2014 period. The global average of each aerosol component is labeled at the top-right of each subgraph, and its contribution to the total AOD is labeled in parenthesis. AOD, aerosol optical depth.

($B = -1.25$), suggesting that the model can capture the regional variability and magnitude of the three aerosol compositions (BC, OC, and sulfate) from the observations.

3.3. Aerosol Optical Depth

3.3.1. Species AOD

Figure 5 shows the annual average AOD of dust, sea salt, carbonaceous, and sulfate aerosols during the 2002–2014 period. High AOD values (>0.2) for dust aerosols are found in the main dust emission source regions which have been mentioned previously, such as North Africa and East Asia. The plumes are found in the downwind direction of the dust source regions, indicating that dust aerosols can be transported to the mid-Atlantic and western Pacific and even across the ocean to the South American continent. For sea salt aerosol, a high-value band appears in the mid-high latitudes of the Southern Hemisphere, which is related to surface wind. Since the carbonaceous aerosols in our model are internally mixed, the optical properties of the black carbon and organic carbon could not be separated. Carbonaceous aerosols are prominent in South America, Central and South Africa, and Southeast Asia, with maximal AOD values of >0.15. The high AOD (>0.3) for sulfate in East Asia and South Asia is obvious, which can be mainly attributed to the rapid industrialization process and the high consumption of fossil fuels (Hoesly et al., 2018; van Marle et al., 2017). The lower AOD of the sulfates is located in industrialized and developed areas such as eastern America and Europe.

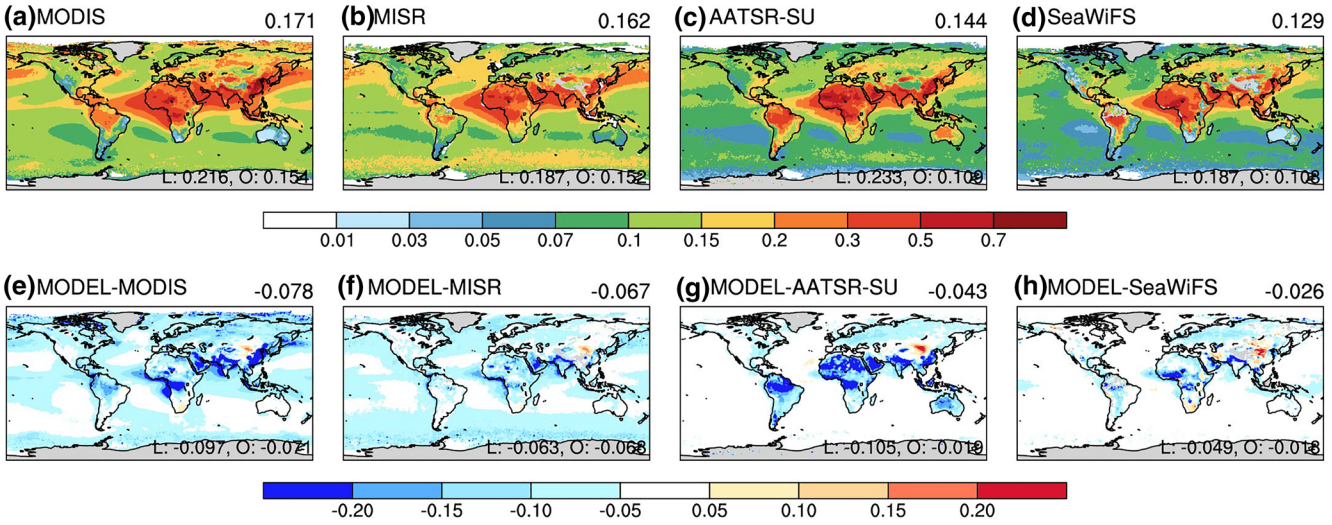

Figure 6. (a–d) Multiyear averaged AOD from MODIS, MISR, AATSR-SU and SeaWiFS and the (e–h) absolute differences between the modeled AOD and MODIS, MISR, AATSR-SU, and SeaWiFS in clear sky conditions. L: Land mean, O: Ocean mean. The global annual mean is shown at the top-right of each subplot. AATSR, Advanced Along-Track Scanning Radiometer; AOD, aerosol optical depth; SeaWiFS, MISR, Multi-angle Imaging Spectroradiometer; MODIS, Moderate Resolution Imaging Spectroradiometer; Sea-viewing Wide Field-of-view Sensor; SU, Swansea algorithm.

3.3.2. Comparisons With Multisource Satellites

Figure 6 shows the multiyear average AOD from (a) MODIS, (b) MISR, (c) AATSR-SU, and (d) SeaWiFS and the absolute difference between the modeled AOD and the four satellite AOD products. To compare the modeled AOD with the satellite AOD, we should principally select the satellite observation time and the observation range under clear sky conditions in the model. Some studies (Colarco et al., 2010) have pointed out that the diurnal variation in AOD is negligible compared with sampling the model with satellite observations under clear sky conditions. Therefore, only the modeled AOD from days with clear sky conditions is used in this study. In addition, it is noticed that the definition of the clear sky condition between the model and the satellite is different, and the model screening clear sky when the whole layer of cloud amount in the model grid is less than 0.2. In general, the spatial distribution of AOD is consistent for all satellite AODs, especially in regions with large magnitudes of AOD, such as East Asia, South Asia, the Middle East, and North Africa, while there are significant differences over the ocean. MODIS and MISR AODs are both higher than those from AATSR-SU and SeaWiFS. Some research has pointed out that MODIS and MISR could be contaminated with clouds (e.g., cirrus, stratocumulus, and broken cumulus clouds), especially at mid-high latitudes (Toth et al., 2013). Although the updated MISR V23 data set has screened high-AOD retrieval blunders caused by cloud contamination over dark water, some known issues and limitations still exist (Witek et al., 2018). Another obvious difference could be seen between AATSR-SU and the other three satellites on land, especially on bright land surfaces (such as North Africa). Bevan et al. (2012) also pointed out that the AATSR-SU overestimated the North African regional AOD compared with AERONET. This may be caused by the land algorithm used in AATSR, which uses a surface model that lacks a priori information about the spectral properties (North et al., 1999).

The differences in AOD between the model and satellites (Figures 6e–6g) show that the modeled AOD is lower in some continental regions, especially East Asia, northern India, the Middle East, and the western coast of Central Africa, but higher on the Asian Gobi Desert. The modeled AODs over the ocean are consistent compared with AATSR-SU and SeaWiFS, and underestimations relative to MODIS and MISR are expected.

Overall, the global mean differences between the model and the satellites are −0.078, −0.067, −0.043, and −0.026. Figure 7 shows the spatial difference in AOD in the different seasons. The maximum positive bias in the Gobi Desert occurs in MAM and JJA, and the maximum negative bias in the Middle East occurs in DJF and MAM. Large negative biases are found over Central Africa and central North Africa in MAM and

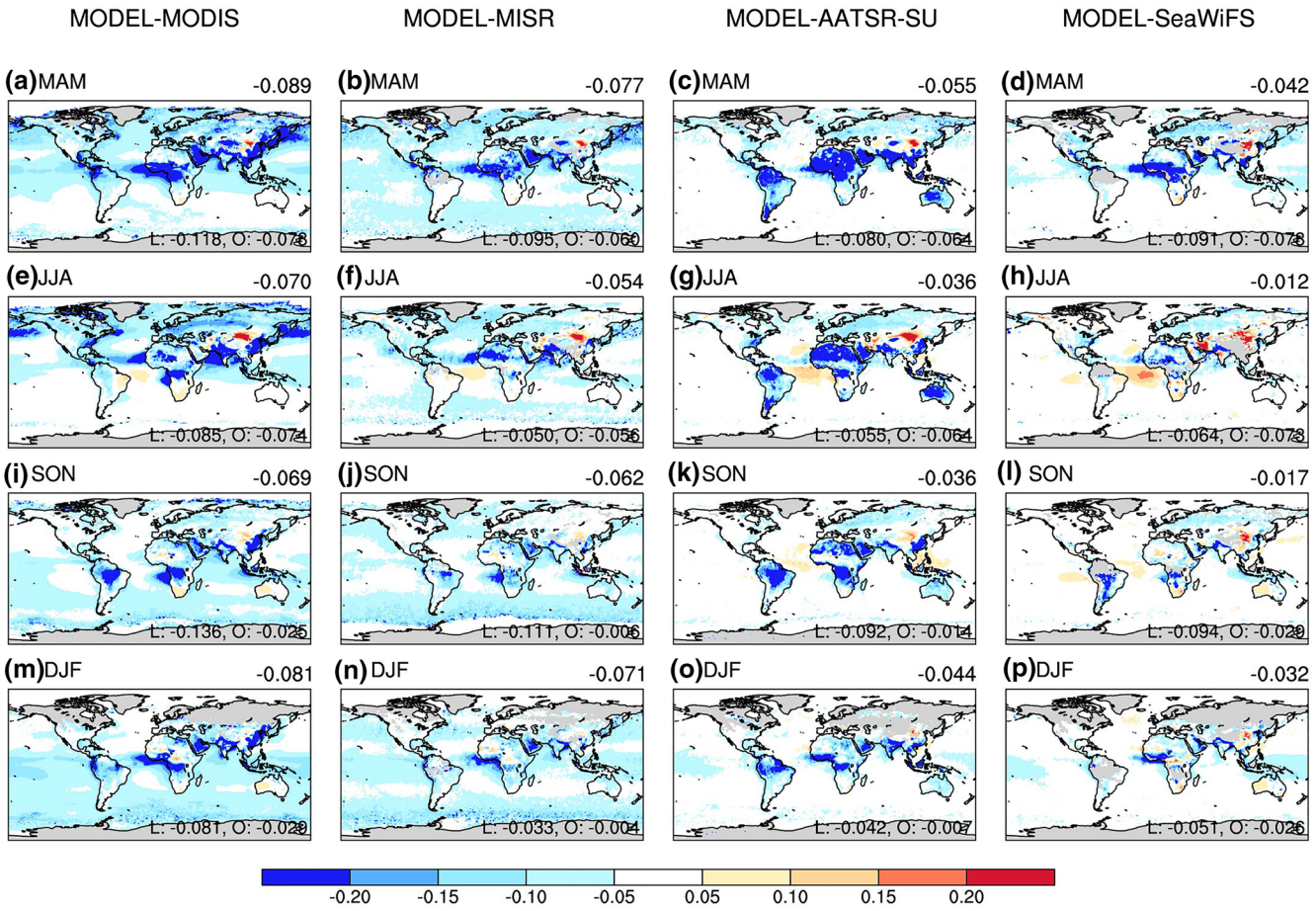

Figure 7. The seasonal mean differences between the modeled AOD and MODIS (a, e, i, and m), MISR (b, f, j, and n), AATSR-SU (c, j, k, and o) and SeaWiFS (d, h, l, and p). The global annual mean is shown at the top-right of each subplot. L: Land mean, O: Ocean mean. AATSR, Advanced Along-Track Scanning Radiometer; AOD, aerosol optical depth; SeaWiFS, MISR, Multi-angle Imaging Spectroradiometer; MODIS, Moderate Resolution Imaging Spectroradiometer; Sea-viewing Wide Field-of-view Sensor; SU, Swansea algorithm.

JJA, respectively. South America and South Africa also show great negative bias in SON during the biomass burning season. The difference between the model and the satellites in the other areas is less than 0.1 in almost all the seasons.

Some biases in dust source regions (e.g., Asia Gobi Desert, Middle East and central North Africa), may be attributed to the bias in the dominant dust aerosol. The dust emission mass flux is calculated for each model time step with the parameterization scheme according to Equation 1 (Dai et al., 2018; Takemura et al., 2000).

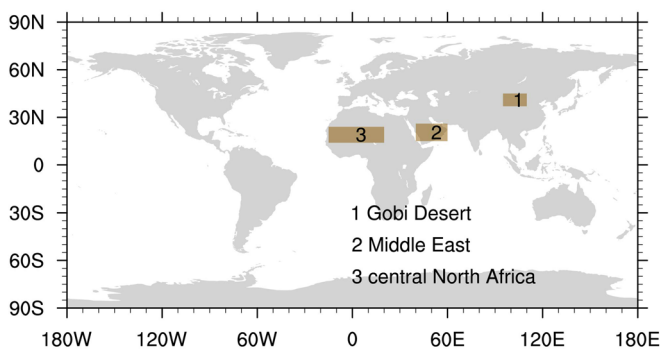

Figure 8. Three dust source areas were selected in this study (1, Gobi Desert; 2, Middle East; 3, central North Africa).

In this study, the simulation performed in this study is an AMIP-like experiment, which is forced by the prescribed monthly sea surface temperature (SST) and not nudged with any meteorological factors. Therefore, the biases in wind speed and soil moisture between the model and observation are expected. Three dust source areas (the Gobi Desert, Middle East, and central North Africa) are selected (Figure 8). Figure 9 shows the multiyear mean results by comparing the daily model output and daily NCEP reanalysis data of the wind speed and soil moisture in these dust source areas. The monthly variations in the modeled wind speed and soil moisture are consistent with the NCEP data in most areas, while the model overestimates the wind speed at a 10 m height (Figures 9a–9c) and underestimates the soil moisture (Figures 9d–9f) systematically in all the

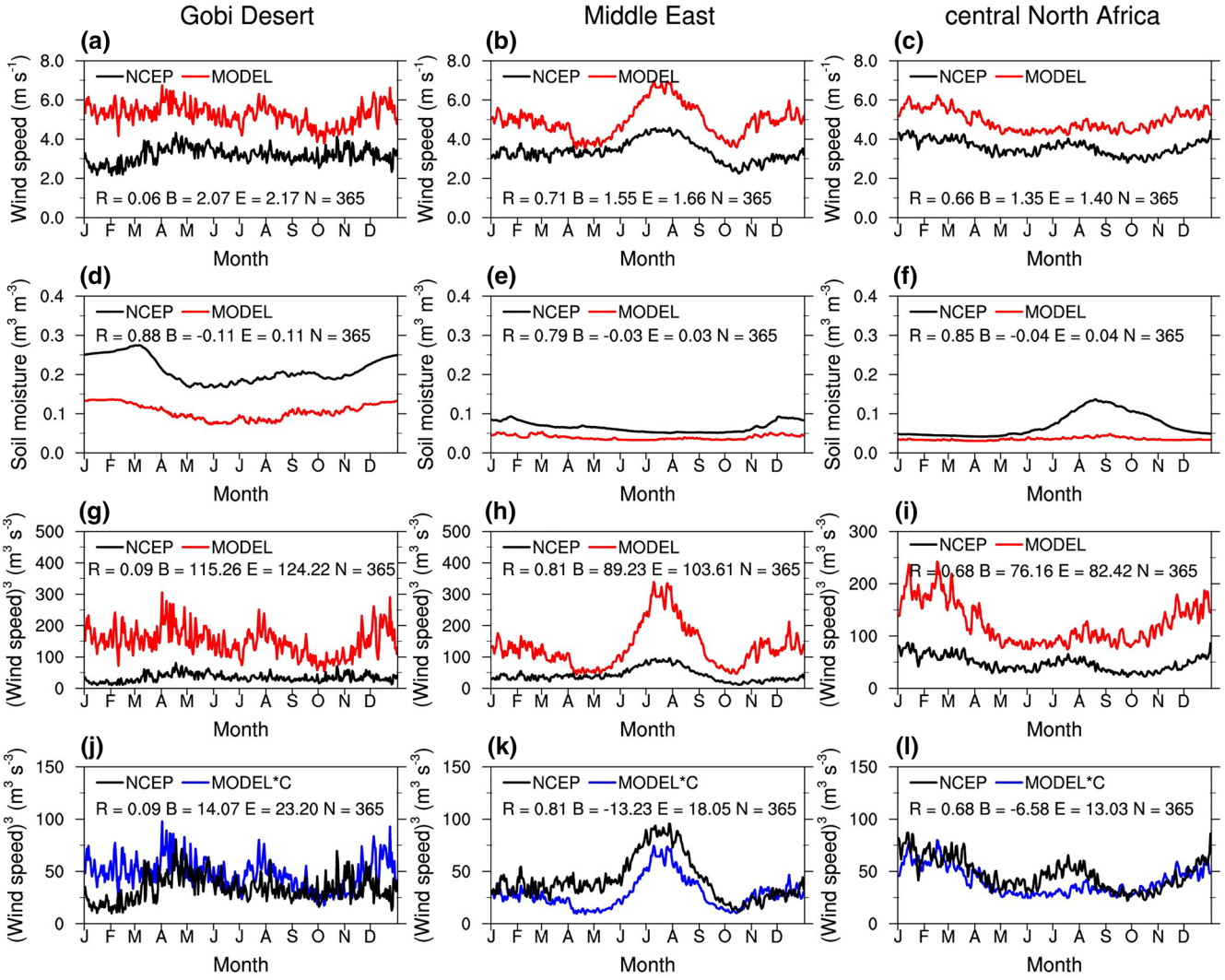

Figure 9. Comparison with the daily model output and daily NCEP reanalysis data in dust source areas (Gobi Desert, Middle East, and central North Africa). (a–c) Wind speed at 10 m height, (d–f) soil moisture, (g–i) cube of wind speed at 10 m height, and (j–l) cube of wind speed at a 10 m height but the model tuned with coefficient *c*.

months in the three dust source areas. According to Equation 1, the emission flux of dust mainly depends on the cube of wind speed, therefore, the emission flux of dust can be simplified as the cube of wind speed multiplied by the tuning coefficient *C*. If we do not consider *C*, that is, *C* is constant 1, the cube of wind speed is depicted in Figures 9g–9i, it shows that all model values (red line) are larger than the NCEP values (black line), which implies that the modeled AOD would be overestimated significantly in these dust source areas. It should be noted that the tuning coefficient *C* in Equation 1 depended on the different dust source areas, which are set to the value of 1.0, 2.0, and 2.0 in Dai et al. (2018). To make the modeled AOD comparable to the observations, that is, making the red line close to the black line in Figures 9g–9i. *C* is reduced to 0.32, 0.22, and 0.33 for the Gobi Desert, Middle East, and central North Africa in this study, which is shown in Figures 9j–9l. Although the dust emission in the tuned model (Figures 9j–9l, blue line) maintains the same level as the reanalysis results (Figures 9j–9l, black line), biases still exist in some seasons. The maximum positive bias in the Gobi Desert occurs in MAM and JJA (Figure 9j), while the maximum negative bias in the Middle East occurs in DJF and MAM (Figure 9k), and the maximum negative bias in central North Africa occurs in MAM and JJA (Figure 9l), which are consistent with the biases of the AODs in these regions (Figure 7). In addition, since most areas in the Gobi Desert in DJF do not satisfy the conditions that the snow amount in dust emission areas should be less than 2 kgm^{-2}, the biases in the dust emissions

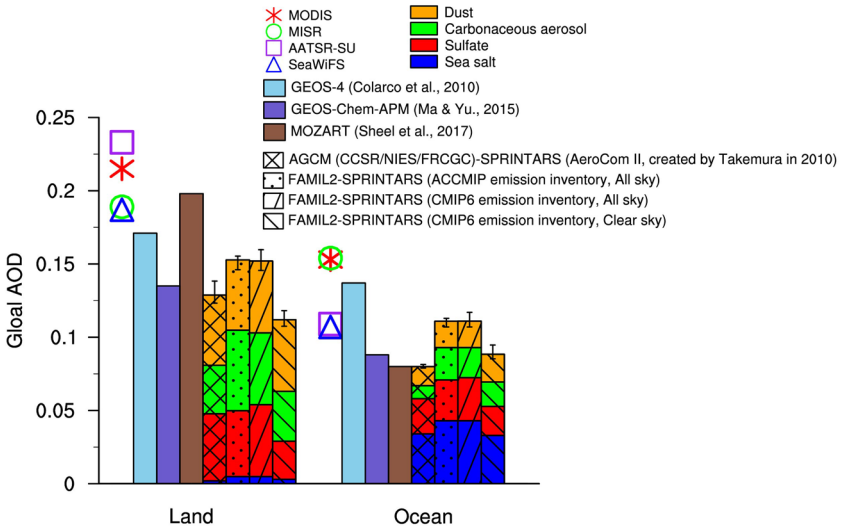

Figure 10. Comparison of the global AODs between the models and multisource satellites retrieved for land and ocean. ACCMIP emission inventory, Emissions for the Atmospheric Chemistry and Climate Model Intercomparison Project; CMIP6 emission inventory, Community Emissions Data System (CEDS) for CMIP6. AOD, aerosol optical depth; CMIP, Coupled Model Intercomparison Project.

induced by the bias of wind speed are negligible. Therefore, we can infer that the tuning coefficient C is the main reason for the overestimation of dust AOD in the Gobi Desert and underestimation of dust AOD in the Middle East and North Africa. The dust emission mass flux is affected nonlinearly by wind speed (roughly cubic relationship) and linearly by C. Therefore, it is insufficient to tune the dust emission mass flux F only with the coefficient C when the modeled wind speed is poorly consistent with the observations.

Figure 10 shows a general overview of the comparison of the climatologically averaged AODs between the models and satellites over land and ocean. The modeled all-sky AOD values (FAMIL2-SPRINTARS, CMIP6 emission, all sky) are higher than the modeled clear sky AOD (cloud amount less than 0.2 defined in the model) (FAMIL2-SPRINTARS, CMIP6 emission, all sky), which are mainly due to higher ambient RH under all sky condition. It should be noted that the satellite monthly mean values are averaged from the observation time when the satellite overpassed under clear sky conditions, and data may be missing in the polar region, but the model AOD means are averaged in all grids in every step time with cloud cover of less than 0.2. This may lead to the discrepancy between the model and the satellites. Over land, all models except MOZART significantly underestimate the AOD values. Comparing AGCM (CCSR/NIES/FRCGC)-SPRINTARS and FAMIL2-SPRINTARS (CMIP6 emission, all sky) in the same simulation period of 2002–2008, although both of them are coupled with the global aerosol model SPRINTARS, FAMIL2-SPRINTARS (CMIP6 emission, all sky) displays better agreement with the satellite AOD. To further analyze the difference in AOD, another experiment of FAMIL2-SPRINTARS (ACCMIP emission, all sky) using the same emission inventories as AGCM (CCSR/NIES/FRCGC)-SPRINTARS is performed. The relative difference in emissions between BC, OC, and SO_2 are 14%, −5%, and 12% according to the comparison of CMIP6 with the ACCMIP emission inventory (Table 3), which contribute to a weak difference in the modeled AOD. Comparing AGCM (CCSR/NIES/FRCGC)-SPRINTARS with FAMIL2-SPRINTARS (ACCMIP emission, all sky), the latter has larger carbonaceous AOD, which is mainly due to the updated larger extinction coefficient of carbonaceous aerosols (Dai et al., 2014) used in the current SPRINTARS model. Over the ocean, it is expected that the carbonaceous AOD values of FAMIL2-SPRINTARS (ACCMIP emission, all sky) could be larger than those from AGCM (CCSR/NIES/FRCGC)-SPRINTARS. Because the emission flux of sea salt is nonlinearly affected by the wind speed at 10 m height, FAMIL2-SPRINTARS (ACCMIP

Table 3
Comparison of Global Annual Average Emission With the CMIP6 and ACCMIP Emissions Inventories During the 2002–2008 Period

Emission inventory	BC ($Tgyr^{-1}$)	OC ($Tgyr^{-1}$)	SO_2 ($Tgyr^{-1}$)
CMIP6	9.05	33.91	133.82
ACCMIP	7.95	35.86	119.18
CMIP6-ACCMIP	1.10	−1.96	14.64
(CMIP6-ACCMIP)/ACCMIP	14%	−5%	12%

Abbreviations: ACCMIP, Atmospheric Chemistry and Climate Model Intercomparison Project; CMIP, Coupled Model Intercomparison Project.

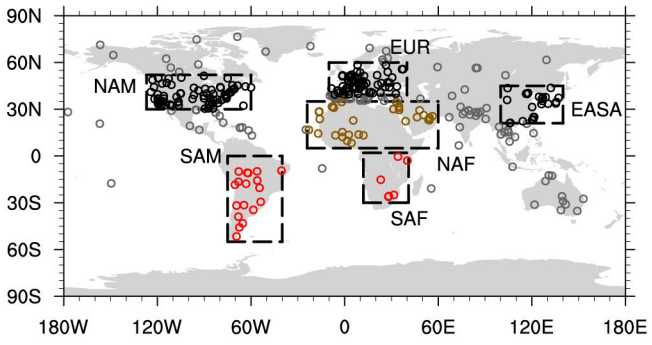

Figure 11. AERONET site locations and six regions used in the study (black, orange, and red represent industrial region, dust region, and biomass burning region, respectively). AERONET, Aerosol Robotic Network.

emission, all sky) produces a larger AOD for sea salt than AGCM (CCSR/NIES/FRCGC)-SPRINTARS, which can be attributed to the modeled wind speed at 10 m height (7.8 ms^{-1}) being larger by ~19% than that of the NCEP reanalysis (6.6 ms^{-1}) over the ocean.

3.3.3. Comparisons With AERONET

Satellite-retrieved AOD has a certain degree of uncertainty, which is related to the surface conditions, cloud screening, aerosol inversion model, and so on (Ma & Yu, 2015). Direct ground-based observations tend to be more accurate. AERONET is one of the longest running and most widely observed global aerosol observation networks, and it can simultaneously retrieve AOD, AE, and SSA.

To further analyze the spatiotemporal variation in AOD, we choose six representative regions and classify them into three groups according to their emission sources (Ma & Yu, 2015), including industrial pollution regions: North America (NAM), Europe (EUR), and East Asia (EASA); dust dominant regions: North Africa (NAF); biomass burning dominant regions: South Africa (SAF) and South America (SAM) (Figure 11). In addition, we also eliminate sites with a small spatial domain (<300 km) and low data quality according to AERONET site assessments (Kinne et al., 2013).

Figure 12 shows a comparison of the model AODs with the AERONET AODs at six areas representing different aerosol regimes. Each panel shows interannual variation, seasonal variation, a scatterplot, and a probability distribution function of the model and AERONET AODs. Over the industrial pollution regions (NAM, EUR, and EASA), sulfate aerosols dominate, and the model can capture the pronounced interannual variations obtained from the AERONET AODs. The simulated AODs are well correlated with the observed AODs, with R values of 0.844 in NAM and 0.564 for EASA, respectively, but with a slight bias (NAM: $B = 0.009$; EASA: $B = -0.062$). The maximum AOD is found in summer, which can be mainly attributed to the large production of sulfate (rich free radicals and water vapors, etc.). In addition, the model underestimates the modeled AOD in EASA and EUR, possibly due to, in part, to the low production of sulfate aerosols (e.g., Goto et al., 2015). Additionally, secondary organic compounds and nitrates are missing in this model (e.g., Shrivastava et al., 2017). Over biomass burning dominant regions, the seasonal cycle of AOD for the model and AERONET in SAM and SAF both indicate that the highest AOD occurs in dry seasons. With respect to the interannual variation in the AERONET AOD, however, the model captures the AOD well in SAM ($R = 0.876$) but fails in SAF ($R = 0.013$). It should be noted that the number of AERONET sites in SAF (6 sites) is less than that in SAM (16 sites), leading to the zone-averaged AOD results being greatly affected by a single site. Additionally, a larger positive bias of the modeled AOD of sulfate aerosols is found in SAF in DJF, which is mainly because half of the AERONET sites in SAF are located in the southernmost part of Africa and are affected by industrial pollution aerosols (Hoesly et al., 2018; van Marle et al., 2017). For the dust dominant region (NAF), the general pattern of modeled AODs is comparable to that of the AERONET observations (NAF: $R = 0.512$) but with a high bias (NAF: $B = -0.076$), especially in the first half of the year. The higher bias can be mainly attributed to the model underestimations of the modeled AOD of the dust in the Middle East in DJF and MAM and central North Africa in MAM by tuning the dust emission coefficients without nudging the wind field, which has been analyzed in detail in section 3.3.2.

3.4. Ångström Exponent

3.4.1. Overall Comparison

In addition to AOD, we also analyze the AE, an important aerosol optical property that characterizes the particle size, calculated in every model time step according to $-\log(\tau_{870nm} / \tau_{440nm}) / \log(\lambda_{870nm} / \lambda_{440nm})$, where τ and λ represent the AOD and wavelengths, respectively. High AE values indicate that the main aerosol components are fine mode aerosols, such as sulfate and/or carbonaceous aerosols. It should be noted that the single species aerosol AE is not affected by its mass content, however, the modeled aerosol AE

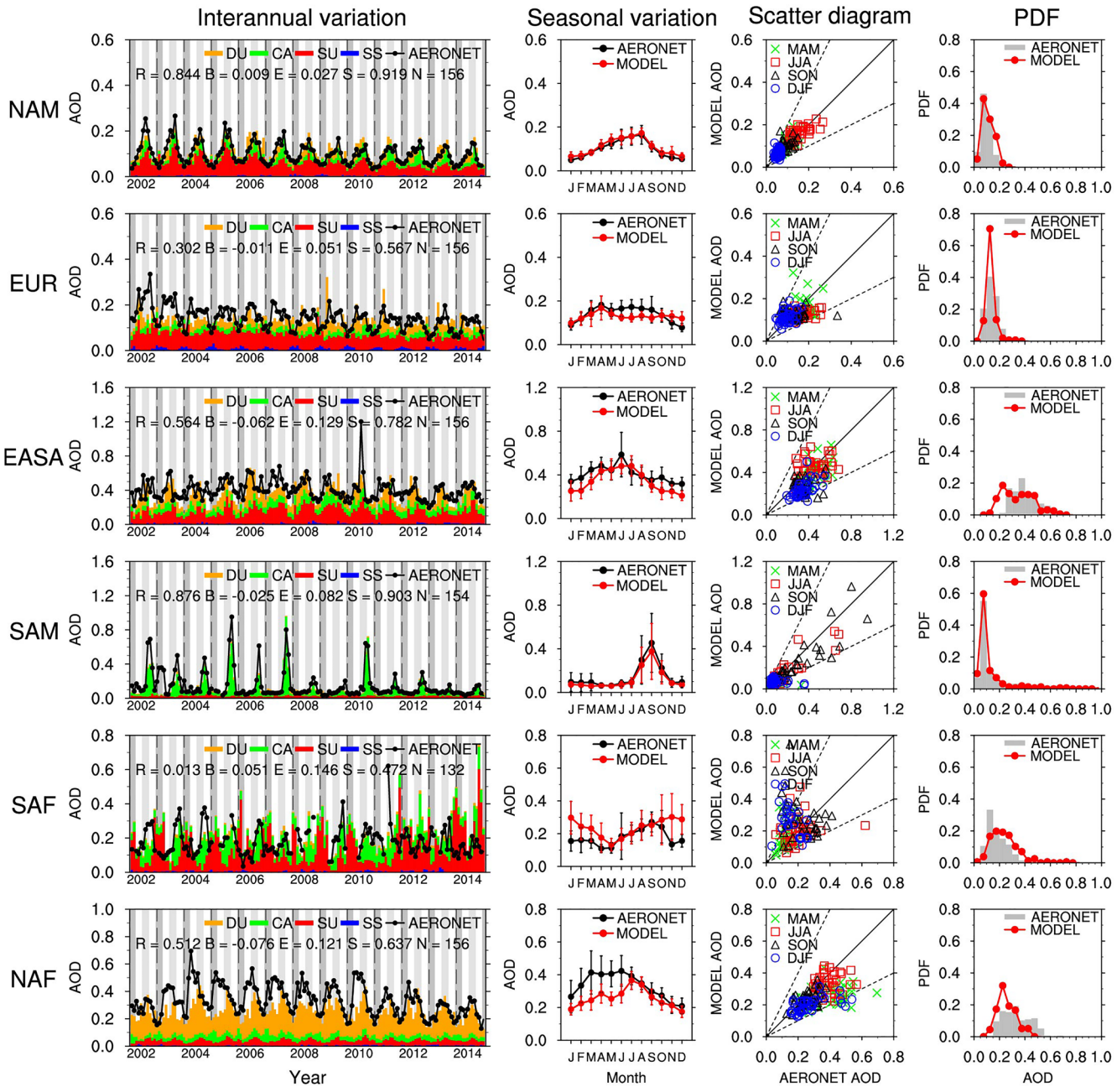

Figure 12. Modeled versus AERONET AODs in the six regions. The panels (from left to right) show a time series, seasonal cycle, scatter diagram, and fractional distribution histogram of the modeled AODs and observed AODs, respectively. The time series of AODs include contributions from each aerosol component and is compared with the observations from 2002 to 2014; light gray and dark gray represent JJA and DJF. The error bars over the curves denote the standard deviations in the seasonal cycle. Points are colored according to the seasons in the scatterplot. CA, carbonaceous aerosol; DU, dust; SU, sulfate; SS, sea salt. R, correlation coefficient; B, absolute bias; E, root mean square error; S, skill score, and N, total number of available observation months. AERONET, Aerosol Robotic Network; AOD, aerosol optical depth.

is calculated by the total modeled AOD at 440 and 870 nm, which may be affected by the difference in the proportion of species content.

Figure 13 shows the modeled AE versus observed AEs from AERONET in the six regions. For the industrial domain areas, the model can capture the overall interannual and seasonal variations in AE, while the modeled AE is systematically lower than the observation. The peak and valley values occur in summer and spring, respectively, mainly because sulfate aerosols are dominant in summer and more dust aerosols

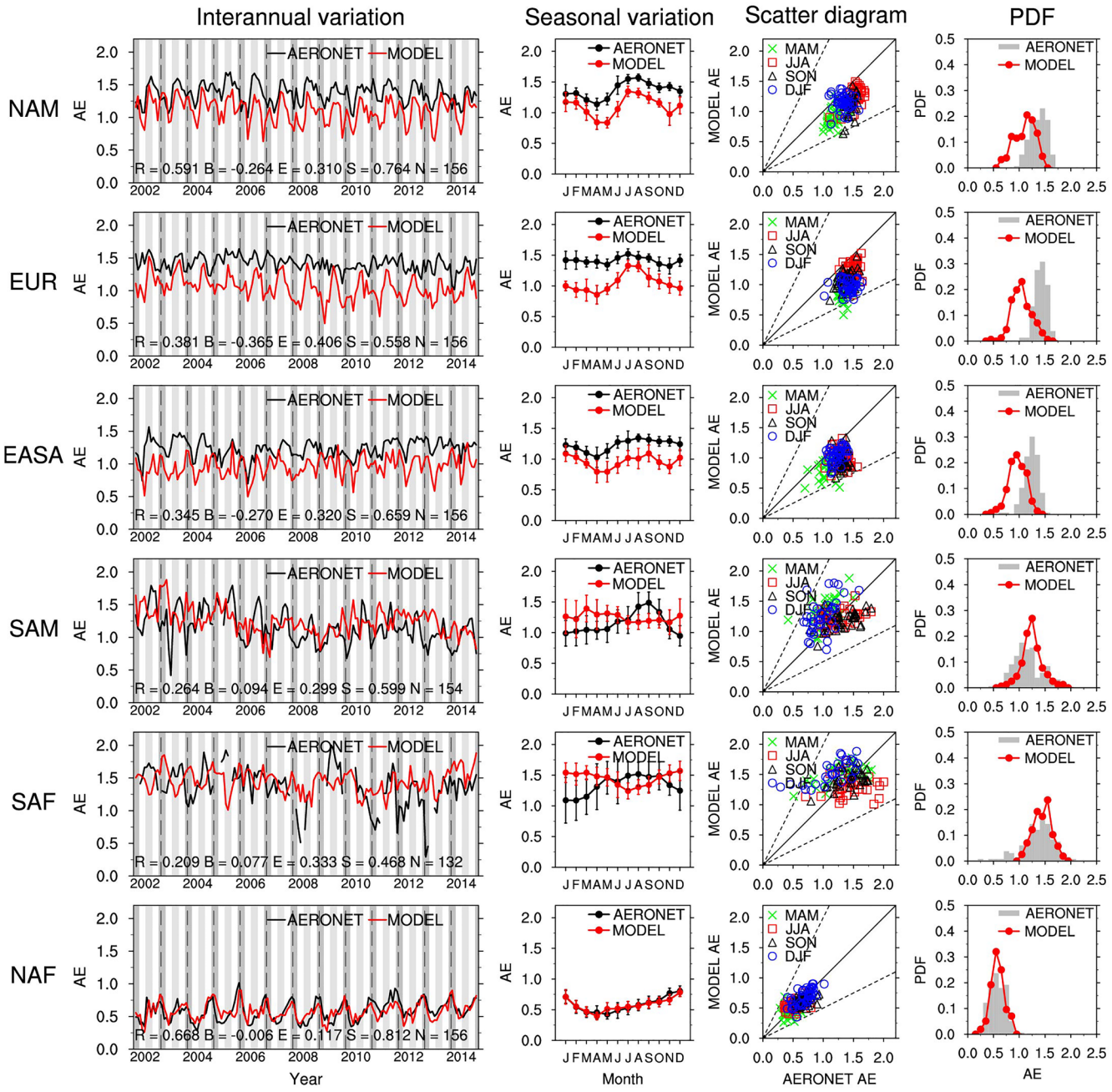

Figure 13. Modeled versus AERONET AEs at six regions. The panel (from left to right) is a time series, seasonal cycle, scatter diagram, and fractional distribution histogram of the model and observations. The time series of AE is compared with the observations from 2002 to 2014. The error bars over the curves denote the standard deviations in seasonal cycle. The points in the scatterplot are colored according to the seasons. AERONET, Aerosol Robotic Network; AE, Ångström Exponent.

are emitted in spring. Over the biomass burning dominant regions, the AERONET AEs present relatively large interannual variation, although it is not successfully being captured in the model. In the Southern Hemisphere, the modeled AE is overestimated in DJF and MAM and underestimated in JJA and SON. The possible reasons for the "antiphase" seasonal variation of AE are analyzed in Section 3.4.2. For the dust dominant region (NAF), the model reproduces the interannual variation fairly well ($R = 0.668$, $B = -0.006$). The model and the observations both show that the maximum occurs in winter and the minimum occurs in spring, which is mainly due to weak dust emissions in winter and strong dust emissions in spring (see Figure 12), leading to a larger proportion of dust in spring and a smaller proportion of dust in winter among

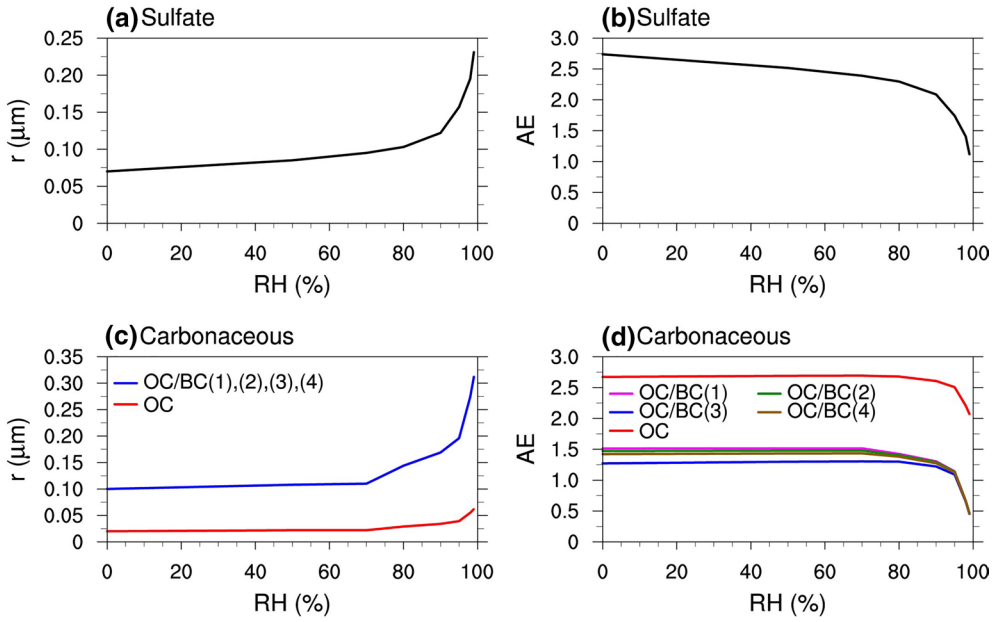

Figure 14. (a and c) The particle radius and (b and d) AE as a function of relative humidity (RH) for sulfate and carbonaceous aerosols, respectively. OC/BC(1), OC/BC(2), OC/BC(3), and OC/BC(4) represent the mass ratio of OC and BC and are 8.28, 6.92, 3.33, and 5.64, respectively. AE, Ångström Exponent.

other aerosol species. In addition, the modeled results agree well with the observations in NAF, implying that the simulated dust particle size distribution using the bins is reasonable.

3.4.2. Bias Analysis

We attempt to find some reasons for the systematic underestimation of the AEs in the industrial areas in the model. Figure 14 shows the particle radius and AE as a function of relative humidity (RH) for sulfate and carbonaceous aerosols, respectively. The AE decreases significantly when RH is greater than 70%, which could be attributed to the hygroscopic growth of the sulfate and carbonaceous aerosols.

Figure 15 shows the comparison between the probability density function (PDF) of the daily modeled RH and daily NCEP reanalysis RH at 850 hPa in the six regions. Over the industrial pollution areas dominated by sulfate and carbonaceous aerosols, the model overestimates the frequency of the modeled RH significantly when the RH is greater than 70%, which could contribute to the underestimation of the AE. In addition, the absence of nitrate aerosols and secondary organic aerosols (SOAs) in the model could also lead to an underestimation of the AE. For biomass burning dominant regions, both the RH of the model and NCEP have the same peak, with modeled values of 60% and 50% for SAM and SAF, respectively, while the model slightly overestimates the modeled RH frequency when the RH is greater than 80%. This may lead to an underestimation of the AE. However, the antiphase relationship of the AE between the model and observations could not be explained reasonably with this "RH effect."

The modeled AE can be affected by the difference in the proportion of species content, and the maximum value of the sulfate aerosol AE (2.74) is much larger than that of the carbonaceous aerosol AE (OC/BC: 1.27–1.54, BC: 1.39, OC 2.67) in the model. We further analyze the proportion of the species in different seasons.

In SAM, although carbonaceous aerosols are dominant (Figure 12), sulfate aerosols are presented in a certain proportion when the total AOD is very low (less than 0.1), and a slight underestimation of the total AOD exists in DJF and MAM. Therefore, we infer that an overestimation of AE is possibly due to a large proportion of sulfate and an underestimation of carbonaceous AOD in DJF and MAM. The observed value of the AE is ~1.5 in September, which is larger than the maximum values of the AE in

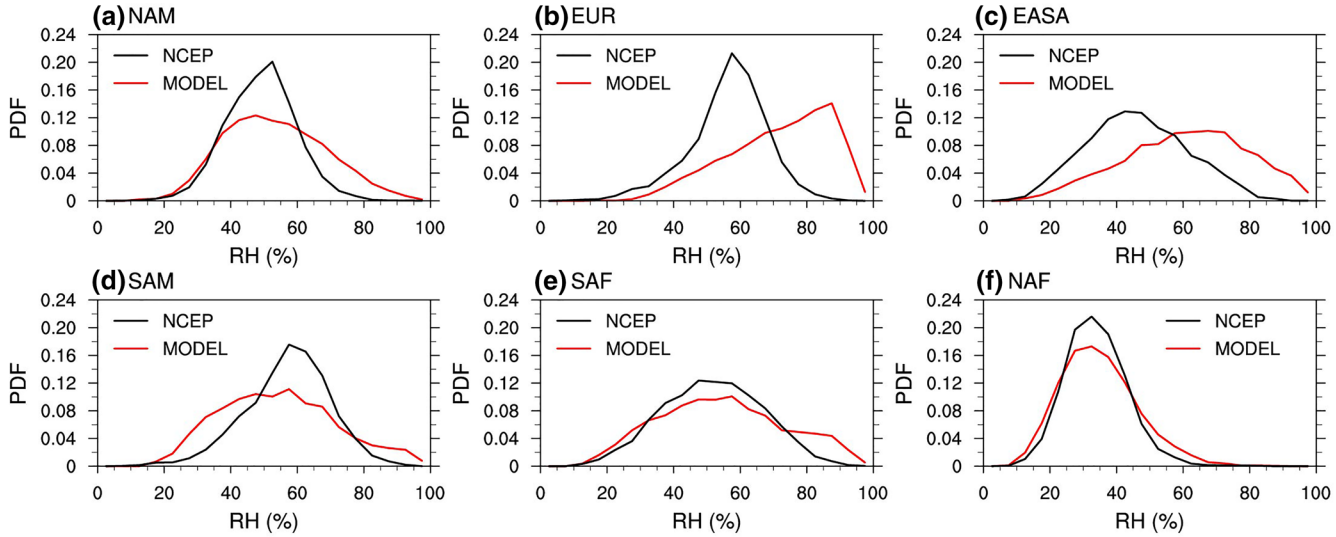

Figure 15. (a-f) The probability density function (PDF) of the modeled daily RH and NCEP reanalysis daily RH at 850 hPa in the six regions.

the carbonaceous aerosol (OC/BC: 1.27–1.54, BC: 1.39), except for OC (2.67). An underestimation of the AE in JJA and SON during the biomass burning season may in part be attributed to the assumption that carbonaceous particle sizes of 0.1 μm are too large in the model relative to those in other studies (e.g., Chin et al., 2009, 0.0212 μm; Heald et al., 2014, 0.064 μm). In SAF, the larger proportion of sulfate aerosols (Figure 12) may partly contribute to the overestimation of the AE in DJF and MAM. Similar to SAM, the larger prescribed carbonaceous particle sizes (0.1 μm) may cause the underestimation of the modeled AE in JJA and SON. For dust-dominant regions, because the dominant dust aerosol is hydrophobic in this study and the RH for the model and NCEP RH are both lower than 70%, the "RH effect" is negligible.

3.5. Single Scattering Albedo

SSA is also an important aerosol optical property that can reflect the scattering capacities of aerosols to visible light at 550 nm, and it is critical for estimating the radiation forcing of aerosols. The spectra of the SSA of the dry particle aerosols for each species are shown in Figure 1, illustrating that scattering aerosols, such as sea salt and sulfate aerosols, scatter almost all visible light with quite weak absorption, dust aerosols exhibit weak absorption, and BC aerosols exhibit strong absorption. The internal mixture of carbonaceous aerosols also reveals a stronger absorption than OC but weaker absorption than BC.

The modeled aerosol SSA is calculated by the total extinction AOD and total scattering AOD (extinction AOD minus absorption AOD) at 550 nm, including all aerosol species in the model. Similar to AE, a single-species aerosol SSA is not affected by its mass content; however, the modeled SSA could be affected by the difference in the proportion of species content.

Figure 16 shows the modeled SSA values versus the AERONET observed SSA values in the six regions. For the industrial domain areas, both the modeled and observed SSA values show weak interannual and seasonal variation, and remain with high (above 0.9) values in NAM and EUR, with low bias (NAM: $B = -0.022$; EUR: $B = -0.007$), which is mainly due to the sulfates AOD being dominant in all seasons (Figure 12). Strong and frequent dust events occur regularly in winter and spring in EASA, which are reflected in the low SSA values and strong interannual and seasonal variation in SSA in both the modeled and observed values. Similarly, in the biomass burning dominant regions, strong biomass burning events occur regularly in the dry season in SAM and SAF, significantly increasing the emissions of absorbing carbonaceous aerosols and sharply decreasing SSA (from ~9.5 to 8.5). For the dust dominant region (NAF), both the model and observations show similar interannual and seasonal variations in SSA. The

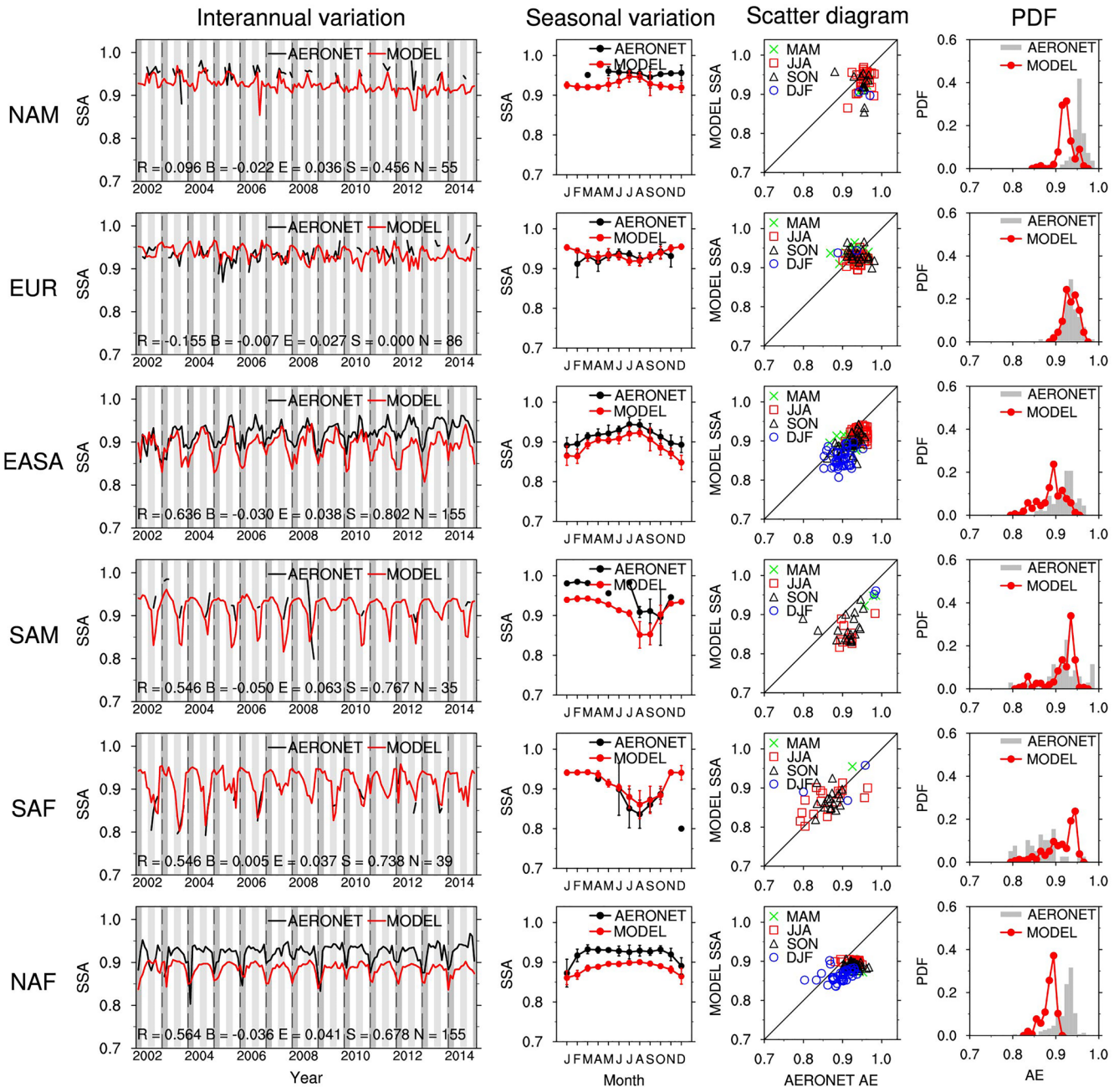

Figure 16. Same as Figure 13 but for AERONET SSA. AERONET, Aerosol Robotic Network; SSA, single scattering albedo.

proportion of dust aerosols in the total aerosols decreases with weak emissions in DJF (Figure 12), leading to an increase in the proportion of carbonaceous aerosols. In addition, a weak peak value of carbonaceous aerosol is also found in DJF (Figure 12), which enlarges the proportion of carbonaceous aerosols, leading to a decrease in SSA. The modeled SSA values are typically 0.04 lower than the observations, indicating that the absorption capacity of the dust aerosols is slightly overestimated in our model. In addition, it is worth noting that the sampling issue is probably also important because the level 2 AERONET inversion data for SSA are valid when the AOD at 440 nm exceeds 0.2. The smaller AOD (<0.2) to some extent can increase the proportion of sulfate in some regions (e.g., EASA, NAF) and lead to a larger SSA relative to the larger AOD (>0.2), which indicates that the simulated SSAs in EASA and NAF may be more underestimated.

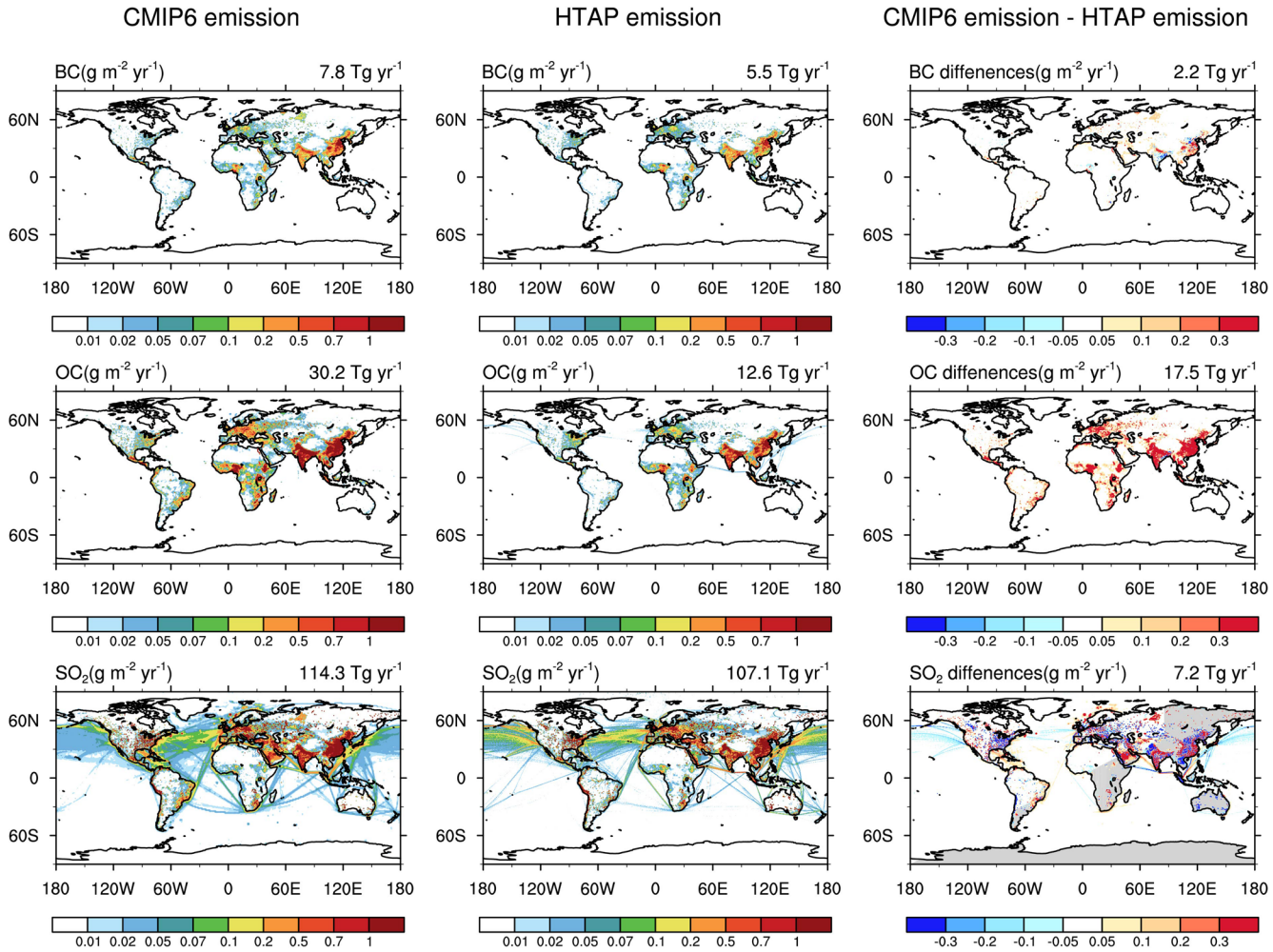

Figure 17. Comparison of annual mean emissions of BC, OC, and SO_2 in the CMIP6 and HTAP emission inventories for 2010. CMIP, Coupled Model Intercomparison Project; HTAP, Hemispheric Transport of Air Pollution.

4. Discussion

4.1. Anthropogenic Emission Inventory

Anthropogenic aerosols are calculated primarily by reading the emission inventory, such as BC, OC, and SO_2 emissions. In our model, we use the CEDS for CMIP6, which is gathered in eight sectors and has a monthly temporal resolution and a spatial resolution of 0.5°. To compare the differences between the different emission inventories, in addition to the CMIP6 emission inventory, we also select the emission inventory of the Hemispheric Transport of Air Pollution, version 2 (HTAP_V2). The HTAP_V2 data set uses the latest national emissions data for 2008 and 2010, and has a monthly temporal resolution and a spatial resolution of 0.1°, which is recommended as the global emissions baseline (Janssens-Maenhout et al., 2015).

Figure 17 shows the comparison of BC, OC, and SO_2 annual mean emissions in CMIP6 and HTAP for 2010. The spatial distributions of the emissions in the two emission inventories are very similar. The main anthropogenic emissions are concentrated in eastern China, northern India, and Europe and the eastern United States, however, there are still some obvious differences. Overall, the CMIP6 emissions are stronger than those of the HTAP, especially for BC (40% higher) and OC (139% higher). The difference in SO_2 emissions is the smallest, at only 8% higher, but in East Asia, northern India, and the Middle East, the difference is still clear.

Interestingly, although we choose a stronger CMIP6 emission inventory in the previous assessment of the modeled AOD with multisource satellites and AERONET observations, we find that the model still tends to

underestimate the AOD values in East Asia and northern India. If we use the HTAP emissions, the simulated negative bias would be greater than that of the CMIP6 emissions. This seems to be more reasonable for the CMIP6 emission in our model. In the meantime, for the OC emission, there is such a large difference between the two emission inventories that further research is urgently required to reduce uncertainty.

4.2. Impacts of Meteorological Fields on Simulated AOD, AE, and SSA

In this study, an AMIP-like simulation causes unrealistic wind fields in dust source regions and biased RH fields in industrialized regions relative to the reanalysis meteorological fields. These biases may be related to any deficiencies in the host atmospheric model FAMIL2. How strong is the biased meteorology impact on aerosol simulation and how large is its contribution to aerosol biases? Here, we further quantify the contribution of meteorological fields to the biases of modeled aerosol properties by performing two additional sets of offline sensitivity experiments over 2002–2014. The two additional experiments read the wind speed at 10 m height and RH fields from NCEP/NCAR reanalysis 1 data set, respectively (https://www.esrl.noaa.gov/psd/data/gridded/data.ncep.reanalysis.html). The reanalysis fields are four times every day (00, 06, 12, 18), which are linearly interpolated to the model grids in every integration time step (i.e., 30 min).

Figure 18 shows the impacts of wind speed at 10 m height (WS10) on the simulated global aerosol optical properties (AOD, AE, and SSA). "Online" and "Offline" represent the original AMIP-like simulation and reanalysis data set diagnosis simulation, respectively. The simulated WS10 in the AMIP-like simulation is generally larger than that of the reanalysis data with global mean difference as of +1.0 ms^{-1} (Figures 18a–18c). The WS10 mainly impacts on dust and sea salt aerosols (Figures S1c, S1f, S1i, and S1l). Stronger wind speeds lead to larger emission fluxes of dust and sea salt aerosols, subsequently higher AOD over the dust dominated regions (Figures S1a–S1f), and smaller AE (more coarse particles) in the North Hemisphere (NH) (Figure 18i). A weak increase in SSA indicates that the biases of wind fields have little impact on the SSA (Figure 18l).

Figure 19 shows the impacts of the WS10 on the regional monthly mean aerosol optical properties (AOD, AE, and SSA) in six different regions. In NH, such as NAM, EUR, and EASA, a weaker dust emission in the "Offline" experiment (blue line in Figure 19) leads to a slight decrease in AOD but a significant increase in AE, implying that the dust aerosol is partly responsible for the underestimation of AE over the industrial dominant regions. For the NAF, although the "Offline" experiment systematically underestimates the dominated dust AOD, the seasonal variations can be better reproduced with a higher correlation coefficient as 0.918 relative to that of the "Online" experiment (red line). The systematical negative biases in dust dominant AOD and positive biases in AE can be tuned with the larger dust tuning coefficient C.

In our model, for the hydrophilic aerosols, such as sulfate and carbonaceous aerosols (except pure BC), their physical and optical properties can be changed by hygroscopic growth. A larger RH generally strengthens the extinction ability of hydrophilic aerosol particles and enlarges their size, that is, it induces the larger AOD and smaller AE. In addition, a larger RH can also enhance the scattering ability of hydrophilic carbonaceous aerosols, which means that the value of the SSA will become larger.

Similar to the above analysis about the wind fields but for the RH fields, Figure 20 shows the impacts of the RH fields on the simulated global aerosol optical properties (AOD, AE, and SSA). The RH values that are lower than 70% from the simulation and the NCEP/NCAR reanalysis 1 data set are both excluded in the comparison. Obviously, the simulated RH at 850 hPa in the AMIP-like simulation is generally larger than that of the reanalysis data with global mean difference as of +4.7% (Figures 20a–20c). The overestimated RH induces the significant increase of hydrophilic aerosol AOD with global mean difference as of +0.035 (Figure 20f), especially in the industrialized regions and biomass burning dominant regions. The global mean species AODs are with differences as +0.012, +0.009, and +0.014 for the sea salt, carbonaceous, and sulfate aerosols, respectively (Figures S2f, S2i, and S2l). The slight decrease in AE (absolute difference = −0.048; relative difference = −6.0%) reveals that RH fields exert weak impacts on the AE (Figure 20i). The increased SSA ranges from about 0.02 to 0.05 in biomass burning dominated regions with the global mean value as of 0.014, suggesting that the biases of RH fields also have weak impacts on the SSA (Figure 20l).

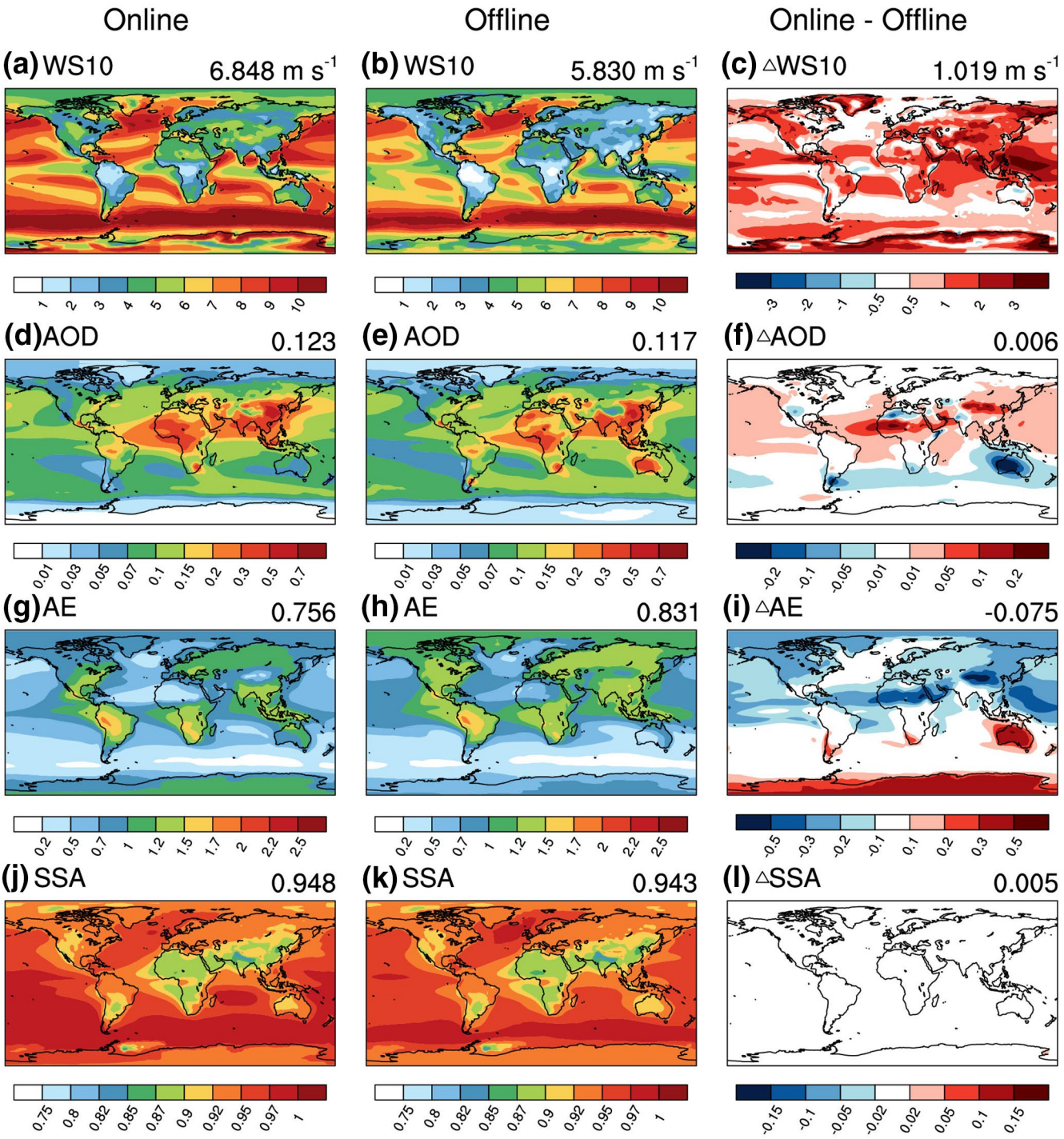

Figure 18. (a-c) The global distribution of modeled annual mean wind speed at 10 m height (WS10), (d-l) aerosol optical properties (AOD, AE, and SSA) from 2002 to 2014. (d-f) AOD, (g-i) AE, (j-l) SSA."Online" and "Offline" represent the original AMIP-like simulation and NCEP reanalysis data set diagnosis simulation, Δ = the variate (WS10, AOD, AE, and SSA) difference between the "Online" and "Offline." The global annual mean is shown at the top-right of each subplot. AE, Ångström Exponent; AOD, aerosol optical depth; SSA, single scattering albedo.

Figure 21 shows the impacts of the RH fields on the regional monthly mean aerosol optical properties (AOD, AE, and SSA) in six different regions. RH mainly impacts the sulfate, carbonaceous, and sea salt aerosols. In the industrial dominant areas, the lower RH induces a significant decrease of AOD in the "Offline" experiment (blue line), which reveals that the RH fields are partly responsible for the biases of AOD.

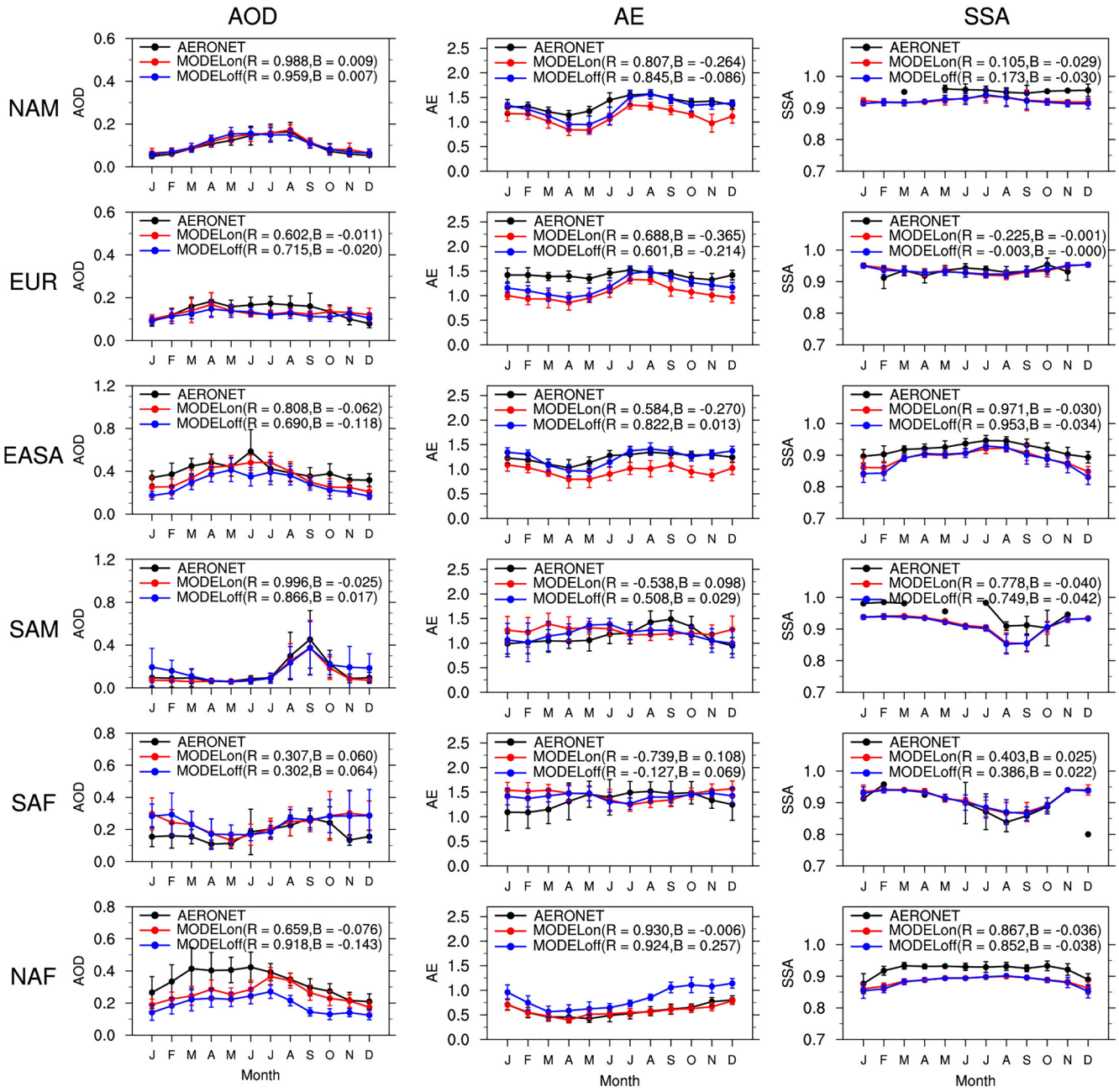

Figure 19. The seasonal variation of modeled aerosol optical properties (AOD, AE, and SSA) in six different regions. The error bars over the curves denote the standard deviations in the seasonal cycle. "MODELon" and "MODELoff" represent the original AMIP-like WS10 (wind speed at 10 m height) simulation and NCEP WS10 reanalysis data set diagnosis simulation, R = correlation coefficient, B = absolute bias. AE, Ångström Exponent; AOD, aerosol optical depth; SSA, single scattering albedo.

The weak increase in AE and weak decrease in SSA show that the RH fields exert little impact on the AE and SSA. It is noted that the size of the hydrophilic aerosol particles would change to smaller (higher AE) when the RH decreases, while the decreased AODs of hydrophilic aerosols may induce the proportion of dust AOD among the total species content to become larger (lower AE). Therefore, the comprehensive effect causes a slightly weak change in AE. In the biomass burning dominant regions, the "RH effect" is similar to that in the industrial dominant regions, that is, the biased RH fields are mainly responsible for the changes in AOD but weak influence in AE and SSA. Due to the hydrophobic dust aerosols assumed in the model, the RH fields have little impact on the aerosol optical properties over the dust dominant region.

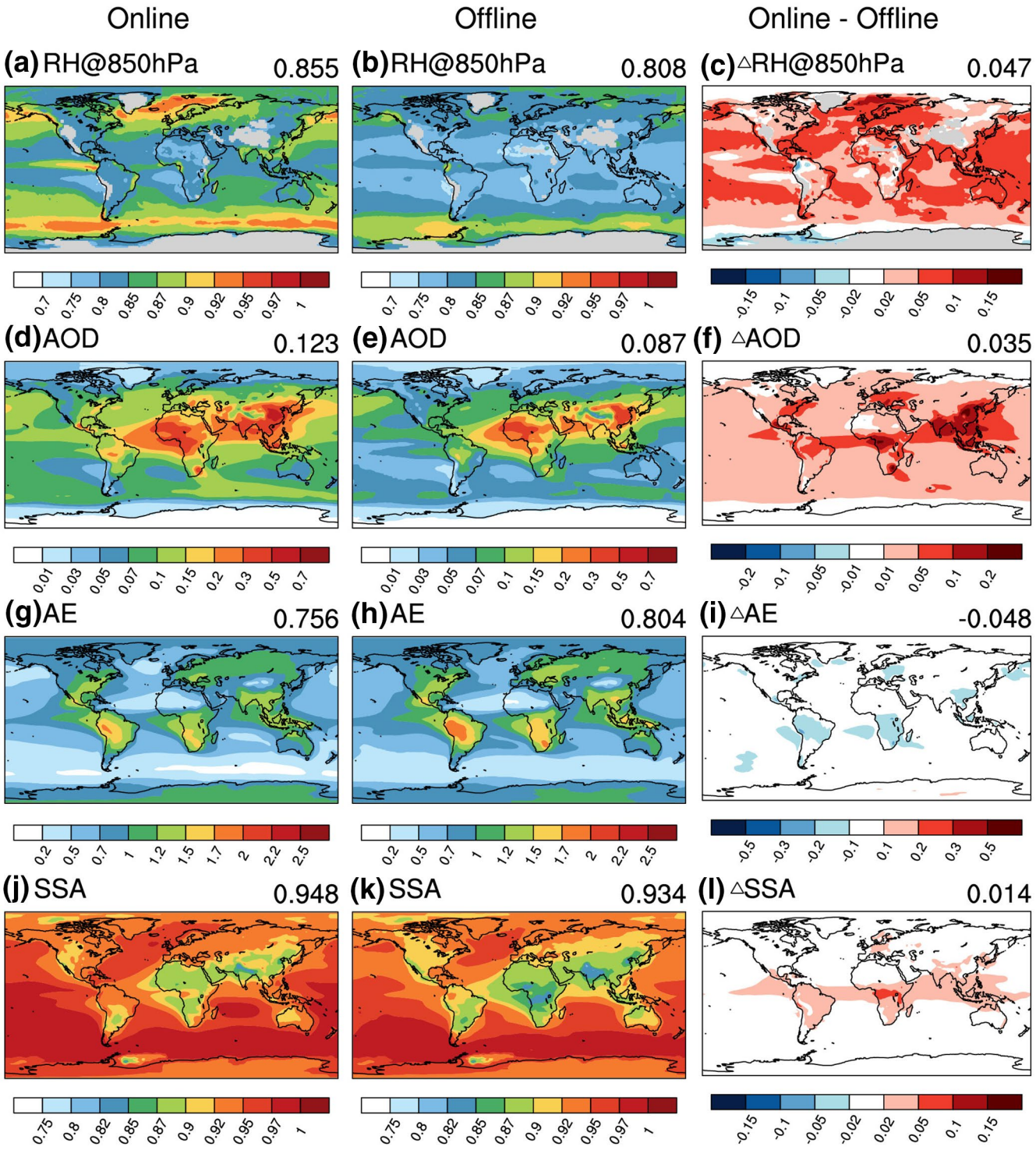

Figure 20. Same as Figure 18 but for relative humility (RH) NCEP reanalysis data set.

Overall, the seasonal variations of AOD in the dust dominant region can be better reproduced with more realistic wind fields at 10 m height relative to that from the AMIP-like simulation. The AEs in the industrial dominant regions are sensitive to the dust aerosol related to the wind fields, implying that the dust aerosol biases (i.e., wind fields biases) are partly responsible for the underestimation of AEs. The AODs in the industrial and biomass burning dominant regions are sensitive to the RH fields. The lower RH induces the

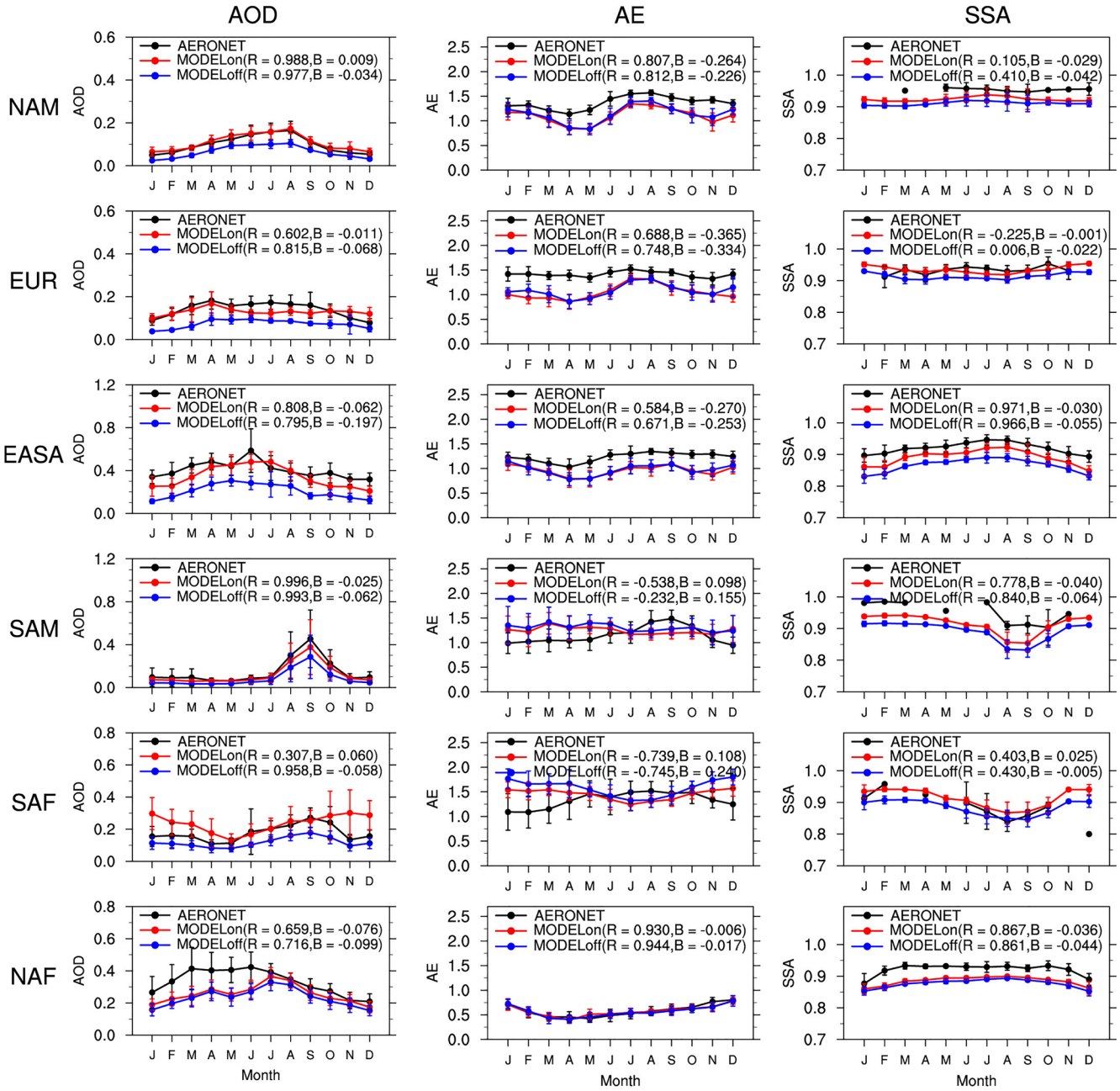

Figure 21. Same as Figure 19 but for relative humility (RH) NCEP reanalysis data set.

decrease in AOD significantly, but with weak changes in AE and SSA. Therefore, it is necessary to reduce the biases of wind fields and RH fields in the model to better simulate the aerosol optical properties.

4.3. Model Development

CAS FGOALS-f3-L is the latest generation GCM, which is developed by LASG/IAP/CAS. A significant advantage is that the dynamical core of FAMIL2 used a finite volume on a cubed-sphere grid (S. J. Lin, 2004; Putman & Lin, 2007) that covers the globe with six tiles, and each tile can contain a minimum of number of grid cells 48 (C48, about 200 km) to a maximum of number of grid cells 1,536 (C1536, about 6.25 km) (J. X.

Li et al., 2017; Zhou et al., 2012). It has continuously contributed to the CMIP from the initial phase to the current phase of the CMIP6 and contributed to the assessment reports of the IPCC (Zhou et al., 2015). The previous version of the CAS-FGOALS-f3-L model reproduced only direct aerosols radiation effect offline and missed the interactions between aerosols and cloud. In this study, we implement an existing aerosol module named SPRINTARS online in the CAS-FGOALS-f3-L (atmospheric component: FAMIL2). Therefore, a new feature of the model is that a higher resolution aerosol simulation can be performed in the FAMIL2, allowing us to conduct more detailed regional studies in complex terrain areas (e.g., Tibet Plateau aerosol transportation) and reproduce the microphysical processes at small scales (e.g., cloud). Another new feature of the model is that the interaction among aerosol, radiation, and cloud has been realized in our model, allowing us to further study aerosol climate effect.

However, some disadvantages of FAMIL2 and SPRINTARS are obvious. First, both the cloud microphysics in FAMIL2 and aerosol microphysics in SPRINTARS still use a single-moment scheme, without prognosing the number concentration of cloud and aerosol particles, despite the fact that most state-of-the-art climate models use double-moment cloud and aerosol microphysics. The size-resolved aerosol microphysics can explicitly reproduce the new particle formation and coagulation and growth processes (e.g., condensation and aqueous sulfate production), therefore, the particle size distribution can be acquired more realistically (Mann et al., 2014). Unphysical characterization of aerosol and cloud with the single-moment can lead to a large uncertainty of interaction between aerosol and cloud in this study. Further work is urgently required to develop size-resolved aerosol microphysics scheme based on current SPRINTARS model and incorporate the double-moment cloud scheme into FAMIL2.

Second, some aerosol species (such as nitrate aerosol and SOA) and online chemically reactive gases are missing in the SPRINTARS, leading to some simulation errors of aerosol physical and optical properties. It is known that the SOA makes up a large portion of fine-mode aerosols in the model. However, the model only treats the SOA from terpene using a single conversion factor, neglecting SOA from other sources (such as isoprene and biomass burning). In addition, it is noticed that the nitrate may account for a greater proportion in the future. Currently, according to the recent AeroCom phase III results, the mean AOD in nitrate is only 0.003, which accounts for roughly 2.3% of the total aerosol AOD, although it cannot be ignored in some local areas. Therefore, a coupled online gas phase chemistry module is required to resolve these missing aerosol species (such as nitrate and SOA) and chemically reactive gases (methane, tropospheric ozone) in the future.

5. Conclusion

We implement an existing aerosol module named SPRINTARS online in the CAS-FGOALS-f3-L and simulate the global aerosol lifecycles and optical properties over the 2002–2014 period using the newer aerosol emission inventories of CMIP6. The simulated surface mass concentrations are compared with ground-based observations. The simulated spatial-temporal distributions of AOD are first evaluated with multi-source satellite retrievals, and the simulated AOD, AE, and SSA are further evaluated with ground-based AERONET measurements. The main findings are listed as follows:

(1) The spatial distributions of the modeled AOD are consistent with all satellite AODs (MODIS, MISR, AATSR-SU, and SeaWiFS). The biases of the AOD, which exist in dust source regions, may be attributed to the biases of the dust aerosol emissions. Through analysis of the dust emission scheme in the three dust source regions (Gobi Desert, Middle East, and central North Africa), it is found that the tuning coefficient C is the main cause of AOD biases when the modeled wind speed exists with large biases
(2) The interannual and seasonal variation of modeled AOD is overall consistent with AERONET observations. However, the model underestimates the modeled AOD in EASA and EUR, possibly due to the lower production of sulfate aerosols and the omission of SOA and nitrate aerosols in the model
(3) Comparing with the AERONET AE, it is found that biases of the simulated dust aerosol are partly responsible for the underestimation of AE over the industrial domain regions (NAM, EUR, and EASA)
(4) The “antiphase” seasonal variation of modeled AE exists in the biomass burning dominant regions (SAM and SAF). An overestimate of AE may be attributed in part to a large proportion of sulfate AOD

in DJF and MAM. In addition, the assumption of a carbonaceous particle size (0.1 μm) is too large in the model relative to other studies (e.g., Chin et al., 2009, 0.0212 μm; Heald et al., 2014, 0.064 μm), which may partly lead to an underestimation of AE in JJA and SON during the biomass burning season

(5) For the dust dominant regions (NAF), the model reproduces the interannual variation of AE fairly well, which implies that the simulated dust particle size distribution is reasonable. However, the values of the modeled SSA are typically 0.04 lower than the observations, indicating that the model slightly overestimates the absorption capacity of dust aerosols at 550 nm and the imaginary part of negative refraction index of dust particles may be larger

(6) Quantifying the contribution of meteorological fields to the biases of modeled aerosol properties. The seasonal variations of AOD in the dust dominant region (NAF) can be better reproduced ($R = 0.918$) with more realistic wind fields at 10 m height relative to that from the AMIP-like simulation. The AODs in the industrial and biomass burning dominant regions are sensitive to the RH fields. The overestimated RH fields induce the significant increase of hydrophilic aerosol AOD with global mean absolute difference (AD) at +0.035 (relative difference (RD) = +40.2%), but exert a weak influence in AE (AD = −0.048; RD = −6.0%) and SSA (AD = +0.014; RD = +1.5%)

These comparisons necessitate model improvements in aerosol size distribution, refractive indices, emissions, and other aspects to better quantify the spatial and temporal distribution of aerosols and study the global climatic effect of aerosols.

Data Availability Statement

The AERONET data are available at https://aeronet.gsfc.nasa.gov/cgi-bin/combined_data_access_inv. The MODIS aerosol products are downloaded from Atmosphere Archive and Distribution System (LAADS) webpage (https://ladsweb.modaps.eosdis.nasa.gov/archive/allData/). The MISR aerosol products are downloaded from https://eosweb.larc.nasa.gov/, The AATSR-SU aerosol products are downloaded from http://www.icare.univ-lille1.fr/, The SeaWiFS aerosol products are downloaded from https://search.earthdata.nasa.gov/. The ACCMIP emission inventories data are available at https://aerocom.met.no/DATA/download/emissions/AEROCOM-II-ACCMIP/ACCMIP/. The CMIP6 emission inventories data are downloaded from https://esgf-node.llnl.gov/search/cmip6/. The HTAP_V2 emission inventories data are downloaded at webpage (https://edgar.jrc.ec.europa.eu/htap_v2/index.php?SECURE=123). The NCEP/NCAR Reanalysis 1 data are obtained from https://www.esrl.noaa.gov/psd/data/gridded/data.ncep.reanalysis.html. The dust and sea salt surface mass concentration data are provided by Huneeus et al. (https://www.atmos-chem-phys.net/11/7781/2011/). The IMPROVE database are available at http://views.cira.colostate.edu/fed/QueryWizard/Default.aspx. The EMEP data set are available at https://projects.nilu.no//ccc/emepdata.html. The aerosol surface mass concentration data for China sites are provided by X. Y. Zhang et al. (https://www.atmos-chem-phys.net/12/779/2012/acp-12-779-2012.html). The CAS FGOALS simulation outputs associated with the work are available at 10.5281/zenodo.3950924.

Acknowledgments
This study is financially supported by the National Natural Science Funds of China (41875133, 41590875, and 41605083), the Youth Innovation Promotion Association CAS (2020078), the Strategic Priority Research Program of the Chinese Academy of Sciences (XDA2006010302), and the National Key R&D Program of China (2017YFC0209803, 2016YFC0202001). The authors thank the AERONET and MODIS, MODIS, MISR, AATSR-SU and SeaWiFS teams for the data used in this study.

References

Abdul-Razzak, H., & Ghan, S. J. (2000). A parameterization of aerosol activation: 2. Multiple aerosol types. *Journal of Geophysical Research*, *105*(D5), 6837–6844. https://doi.org/10.1029/1999jd901161

Bao, Q., Lin, P., Zhou, T., Liu, Y., Yu, Y., Wu, G., et al. (2013). The flexible Global Ocean-Atmosphere-Land system model, spectral version 2: FGOALS-s2. *Advances in Atmospheric Sciences*, *30*(3), 561–576. https://doi.org/10.1007/s00376-012-2113-9

Bao, Q., Wu, G., Liu, Y., Yang, J., Wang, Z., & Zhou, T. (2010). An introduction to the coupled model FGOALS1.1-s and its performance in East Asia. *Advances in Atmospheric Sciences*, *27*, 1131–1142. https://doi.org/10.1007/s00376-010-9177-1

Bao, Q., Wu, X., Li, J., Wang, L., He, B., Wang, X., et al. (2019). Outlook for El Niño and the Indian Ocean dipole in autumn-winter 2018–2019. *Chinese Science Bulletin*, *64*(0023–074X), 73. https://doi.org/10.1360/N972018-00913

Berry, E. X. (1968). Modification of the warm rain process. *1st National Conference on Weather Modification*, New York, NY: American Meteorology Society, 81–85.

Bessho, K., Date, K., Hayashi, M., Ikeda, A., Imai, T., Inoue, H., et al. (2016). An introduction to Himawari-8/9-Japan's new-generation geostationary meteorological satellites. *Journal of the Meteorological Society of Japan. Ser. II*, *94*(2), 151–183. https://doi.org/10.2151/jmsj.2016-009

Bevan, S. L., North, P. R. J., Los, S. O., & Grey, W. M. F. (2012). A global dataset of atmospheric aerosol optical depth and surface reflectance from AATSR. *Remote Sensing of Environment*, *116*, 199–210. https://doi.org/10.1016/j.rse.2011.05.024

Boucher, O., Randall, D., Artaxo, P., Bretherton, C., Feingold, G., Forster, P., et al. (2013). Clouds and aerosols. Climate change 2013: The physical science basis. In *Contribution of working group I to the Fifth Assessment Report of the Intergovernmental Panel on Climate Change* (pp. 571–657). Cambridge University Press.

Bretherton, C. S., & Park, S. (2009). A new moist turbulence parameterization in the community atmosphere model. *Journal of Climate*, *22*(12), 3422–3448. https://doi.org/10.1175/2008jcli2556.1

Cesnulyte, V., Lindfors, A., Pitkänen, M., Lehtinen, K., Morcrette, J.-J., & Arola, A. (2014). Comparing ECMWF AOD with AERONET observations at visible and UV wavelengths. *Atmospheric Chemistry and Physics*, *14*(2), 593–608. https://doi.org/10.5194/acp-14-593-2014

Che, H., Zhang, X., Chen, H., Damiri, B., Goloub, P., Li, Z., et al. (2009). Instrument calibration and aerosol optical depth validation of the China Aerosol Remote Sensing Network. *Journal of Geophysical Research*, *114*, D03206. https://doi.org/10.1029/2008jd011030

Chin, M., Diehl, T., Dubovik, O., Eck, T., Holben, B., Sinyuk, A., et al. (2009). Light absorption by pollution, dust, and biomass burning aerosols: A global model study and evaluation with AERONET measurements. *Annales Geophysicae*, *27*(9), 3439–3464. https://doi.org/10.5194/angeo-27-3439-2009

Chylek, P., & Wong, J. (1995). Effect of absorbing aerosols on global radiation budget. *Geophysical Research Letters*, *22*(8), 929–931. https://doi.org/10.1029/95gl00800

Clough, S., Shephard, M., Mlawer, E. J., Delamere, J. S., Iacono, M. J., Cady-Pereira, K., et al. (2005). Atmospheric radiative transfer modeling: A summary of the AER codes. *Journal of Quantitative Spectroscopy & Radiative Transfer*, *91*, 233–244. https://doi.org/10.1016/j.jqsrt.2004.05.058

Colarco, P., da Silva, A., Chin, M., & Diehl, T. (2010). Online simulations of global aerosol distributions in the NASA GEOS-4 model and comparisons to satellite and ground-based aerosol optical depth. *Journal of Geophysical Research*, *115*, D14207. https://doi.org/10.1029/2009JD012820

Dai, T., Cheng, Y., Zhang, P., Shi, G., Sekiguchi, M., Suzuki, K., et al. (2018). Impacts of meteorological nudging on the global dust cycle simulated by NICAM coupled with an aerosol model. *Atmospheric Environment*, *190*, 99–115. https://doi.org/10.1016/j.atmosenv.2018.07.016

Dai, T., Goto, D., Schutgens, N. A. J., Dong, X., Shi, G., & Nakajima, T. (2014). Simulated aerosol key optical properties over global scale using an aerosol transport model coupled with a new type of dynamic core. *Atmospheric Environment*, *82*, 71–82. https://doi.org/10.1016/j.atmosenv.2013.10.018

Dai, T., Shi, G. Y., & Nakajima, T. (2015). Analysis and evaluation of the global aerosol optical properties simulated by an online aerosol-coupled non-hydrostatic icosahedral atmospheric model. *Advances in Atmospheric Sciences*, *32*(6), 743–758. https://doi.org/10.1007/s00376-014-4098-z

Dubovik, O., Herman, M., Holdak, A., Lapyonok, T., Tanre, D., Deuze, J. L., et al. (2011). Statistically optimized inversion algorithm for enhanced retrieval of aerosol properties from spectral multi-angle polarimetric satellite observations. *Atmospheric Measurement Techniques*, *4*(5), 975–1018. https://doi.org/10.5194/amt-4-975-2011

Dubovik, O., & King, M. D. (2000). A flexible inversion algorithm for retrieval of aerosol optical properties from Sun and sky radiance measurements. *Journal of Geophysical Research*, *105*(D16), 20673–20696. https://doi.org/10.1029/2000JD900282

Dubovik, O., Lapyonok, T., Litvinov, P., Herman, M., & Federspiel, C. (2014). GRASP: A versatile algorithm for characterizing the atmosphere. *SPIE Newsroom*, 5513–5527. https://doi.org/10.1117/2.1201408.005558

Fei, K.-c., Wu, L., & Zeng, Q.-c. (2019). Aerosol optical depth and burden from large sea salt particles. *Journal of Geophysical Research: Atmospheres*, *124*(3), 1680–1696. https://doi.org/10.1029/2018jd029814

Goto, D., Nakajima, T., Dai, T., Takemura, T., Kajino, M., Matsui, H., et al. (2015). An evaluation of simulated particulate sulfate over East Asia through global model intercomparison. *Journal of Geophysical Research: Atmospheres*, *120*(12), 6247–6270. https://doi.org/10.1002/2014jd021693

Goto, D., Nakajima, T., Takemura, T., & Sudo, K. (2011). A study of uncertainties in the sulfate distribution and its radiative forcing associated with sulfur chemistry in a global aerosol model. *Atmospheric Chemistry and Physics*, *11*(21), 10889–11091. https://doi.org/10.5194/acp-11-10889-2011

Harris, L. M., & Lin, S.-J. (2014). Global-to-Regional nested grid climate simulations in the GFDL high resolution atmospheric model. *Journal of Climate*, *27*(13), 4890–4910. https://doi.org/10.1175/jcli-d-13-00596.1

Haywood, J., & Boucher, O. (2000). Estimates of the direct and indirect radiative forcing due to tropospheric aerosols: A review. *Reviews of Geophysics*, *38*(4), 513–543. https://doi.org/10.1029/1999RG000078

Heald, C. L., Ridley, D. A., Kroll, J. H., Barrett, S. R. H., Cady-Pereira, K. E., Alvarado, M. J., et al. (2014). Contrasting the direct radiative effect and direct radiative forcing of aerosols. *Atmospheric Chemistry and Physics*, *14*(11), 5513–5527. https://doi.org/10.5194/acp-14-5513-2014

He, B., Bao, Q., Wang, X., Zhou, L., Wu, X., Liu, Y., et al. (2019). CAS FGOALS-f3-L model datasets for CMIP6 historical atmospheric model intercomparison project simulation. *Advances in Atmospheric Sciences*, *36*(8), 771–778. https://doi.org/10.1007/s00376-019-9027-8

Hoesly, R., Smith, S., Feng, L., Klimont, Z., Janssens-Maenhout, G., Pitkanen, T., et al. (2018). Historical (1750–2014) anthropogenic emissions of reactive gases and aerosols from the Community Emissions Data System (CEDS). *Geoscientific Model Development*, *11*, 369–408. https://doi.org/10.5194/gmd-11-369-2018

Holben, B. N., Eck, T. F., Slutsker, I., Tanre, D., Buis, J., Setzer, A., et al. (1998). AERONET—a federated instrument network and data archive for aerosol characterization. *Remote Sensing of Environment*, *66*(1), 1–16. https://doi.org/10.1016/S0034-4257(98)00031-5

Holzer-Popp, T., de Leeuw, G., Griesfeller, J., Martynenko, D., Kluser, L., Bevan, S., et al. (2013). Aerosol retrieval experiments in the ESA Aerosol_cci project. *Atmospheric Measurement Techniques*, *6*(8), 1919–1957. https://doi.org/10.5194/amt-6-1919-2013

Hooker, S. B., & McClain, C. R. (2000) The calibration and validation of SeaWiFS data. *Progress in Oceanography*, *4135*, 281–293. https://doi.org/10.1117/12.494258

Hsu, N. C., Jeong, M.-J., Bettenhausen, C., Sayer, A. M., Hansell, R., Seftor, C. S., et al. (2013). Enhanced Deep Blue aerosol retrieval algorithm: The second generation. *Journal of Geophysical Research: Atmospheres*, *118*(16), 9296–9315. https://doi.org/10.1002/jgrd.50712

Hsu, N. C., Lee, J., Sayer, A. M., Kim, W., Bettenhausen, C., & Tsay, S. C. (2019). VIIRS deep blue aerosol products over land: Extending the EOS long-term aerosol data records. *Journal of Geophysical Research: Atmospheres*, *124*(7), 4026–4053. https://doi.org/10.1029/2018jd029688

Hunke, E., & Lipscomb, W. (2010). *CICE: The Los Alamos Sea ice model documentation and software user's manual version 4.1*. Tech. Rep, LA-CC-, 06-012, 675.

Janssens-Maenhout, G., Crippa, M., Guizzardi, D., Dentener, F., Muntean, M., Pouliot, G., et al. (2015). HTAP_v2.2: A mosaic of regional and global emission grid maps for 2008 and 2010 to study hemispheric transport of air pollution. *Atmospheric Chemistry and Physics*, *15*(19), 11411–11432. https://doi.org/10.5194/acp-15-11411-2015

Kinne, S., O'Donnel, D., Stier, P., Kloster, S., Zhang, K., Schmidt, H., et al. (2013). MAC-v1: A new global aerosol climatology for climate studies. *Journal of Advances in Modeling Earth Systems*, *5*(4), 704–740. https://doi.org/10.1002/jame.20035

Kittaka, C., Winker, D., Vaughan, M., Omar, A., & Remer, L. (2011). Intercomparison of column aerosol optical depths from CALIPSO and MODIS-Aqua. *Atmospheric Measurement Techniques*, *4*(2), 131–141. https://doi.org/10.5194/amt-4-131-2011

Lamarque, J.-F., Emmons, L., Hess, P., Kinnison, D., Tilmes, S., Vitt, F., et al. (2012). CAM-chem: Description and evaluation of interactive atmospheric chemistry in the community Earth system model. *Geoscientific Model Development*, *5*, 369–411. https://doi.org/10.5194/gmd-5-369-2012

Levy, R., Mattoo, S., Munchak, L., Remer, L., Sayer, A., Patadia, F., et al. (2013). The Collection 6 MODIS aerosol products over land and ocean. *Atmospheric Measurement Techniques*, *6*(11), 2989. https://doi.org/10.5194/amt-6-2989-2013

Levy, R., Remer, L., Kleidman, R., Mattoo, S., Ichoku, C., Kahn, R., et al. (2010). Global evaluation of the Collection 5 MODIS dark-target aerosol products over land. *Atmospheric Chemistry and Physics*, *10*(21), 10399–10420. https://doi.org/10.5194/acp-10-10399-2010

Li, J.-X., Bao, Q., Liu, Y.-M., & Wu, G.-X. (2017). Evaluation of the computational performance of the finite-volume atmospheric model of the IAP/LASG (FAMIL) on a high-performance computer. *Atmospheric and Oceanic Science Letters*, *10*(4), 329–336. https://doi.org/10.1080/16742834.2017.1331111

Li, J., Bao, Q., Liu, Y., Wu, G., Wang, L., He, B., et al. (2019). Evaluation of FAMIL2 in simulating the climatology and seasonal-to-interannual variability of tropical cyclone characteristics. *Journal of Advances in Modeling Earth Systems*, *11*(4), 1117–1136. https://doi.org/10.1029/2018ms001506

Lin, S.-J. (2004). A "vertically Lagrangian" finite-volume dynamical core for global models. *Monthly Weather Review*, *132*(10), 2293–2307. https://doi.org/10.1175/1520-0493(2004)132<2293:avlfdc>2.0.co;2

Lin, Y.-L., Farley, R. D., & Orville, H. D. (1983). Bulk parameterization of the snow field in a cloud model. *Journal of Climate and Applied Meteorology*, *22*(6), 1065–1092. https://doi.org/10.1175/1520-0450(1983)022<1065:bpotsf>2.0.co;2

Liousse, C., Penner, J., Chuang, C., Walton, J., Eddleman, H., & Cachier, H. (1996). A global three-dimensional model study of carbonaceous aerosols. *Journal of Geophysical Research: Atmospheres*, *101*(D14), 19411–19432. https://doi.org/10.1029/95JD03426

Liu, X., Ma, P.-L., Wang, H., Tilmes, S., Singh, B., Easter, R. C., et al. (2016). Description and evaluation of a new four-mode version of the modal aerosol module (MAM4) within version 5.3 of the community Atmosphere model, *Geoscientific Model Development* (Online), *9* (PNNL-SA-110649). https://doi.org/10.5194/gmd-9-505-2016

Ma, X., Bartlett, K., Harmon, K., & Yu, F. (2013). Comparison of AOD between CALIPSO and MODIS: Significant differences over major dust and biomass burning regions. *Atmospheric Measurement Techniques*, *6*(9), 2391–2401. https://doi.org/10.5194/amt-6-2391-2013

Mann, G. W., Carslaw, K. S., Reddington, C. L., Pringle, K. J., Schulz, M., Asmi, A., et al. (2014). Intercomparison and evaluation of global aerosol microphysical properties among AeroCom models of a range of complexity. *Atmospheric Chemistry and Physics*, *14*(9), 4679–4713. https://doi.org/10.5194/acp-14-4679-2014

Martins, J. V., Tanré, D., Remer, L., Kaufman, Y., Mattoo, S., & Levy, R. (2002). MODIS cloud screening for remote sensing of aerosols over oceans using spatial variability. *Geophysical Research Letters*, *29*(12), MOD4-1-MOD4-4. https://doi.org/10.1029/2001gl013252

Martonchik, J. V., Diner, D. J., Kahn, R. A., Ackerman, T. P., Verstraete, M. M., Pinty, B., et al. (1998). Techniques for the retrieval of aerosol properties over land and ocean using multiangle imaging. *IEEE Transactions on Geoscience and Remote Sensing*, *36*(4), 1212–1227. https://doi.org/10.1109/36.701027

Ma, X., & Yu, F. (2015). Seasonal and spatial variations of global aerosol optical depth: Multi-year modeling with GEOS-Chem-APM and comparisons with multiple-platform observations. *Tellus B: Chemical and Physical Meteorology*, *67*(1), 25115. https://doi.org/10.3402/tellusb.v67.25115

Malm, W. C., Day, D. E., Kreidenweis, S. M., Collett, J. L., & Lee, T. (2003). Humidity-dependent optical properties of fine particles during the Big Bend Regional Aerosol and Visibility Observational Study. *Journal of Geophysical Research: Atmospheres*, *108*(D9), 4279. https://doi.org/10.1029/2002JD002998

Malm, W. C., Sisler, J. F., Huffman, D., Eldred, R. A., & Cahill, T. A. (1994). Spatial and seasonal trends in particle concentration and optical extinction in the United States. *Journal of Geophysical Research: Atmospheres*, *99*(D1), 1347–1370. https://doi.org/10.1029/93JD02916

McClain, C. R., Feldman, G. C., & Hooker, S. B. (2004). An overview of the SeaWiFS project and strategies for producing a climate research quality global ocean bio-optical time series. *Deep-Sea Research Part II-topical Studies in Oceanography*, *51*(1–3), 5–42. https://doi.org/10.1016/j.dsr2.2003.11.001

Monahan, E. C., Spiel, D. E., & Davidson, K. L. (1986). A model of marine aerosol generation via whitecaps and wave disruption. In E. C. (Ed.), *Oceanic Whitecaps: And Their Role in Air-Sea Exchange Processes*, Dordrecht, The Netherlands: D. Reidel.

Myhre, G., Samset, B. H., Schulz, M., Balkanski, Y., Bauer, S., Berntsen, T. K., et al. (2013). Radiative forcing of the direct aerosol effect from AeroCom Phase II simulations. *Atmospheric Chemistry and Physics*, *13*(4), 1853–1877. https://doi.org/10.5194/acp-13-1853-2013

Myhre, G., Shindell, D., Bréon, F.-M., Collins, W., Fuglestvedt, J., Huang, J., Koch, D., et al. (2013). Clouds and aerosols. Climate change 2013: The physical science basis. In *Contribution of Working Group I to the Fifth Assessment Report of the Intergovernmental Panel on Climate Change* (pp. 659–740), Cambridge University Press.

Nabat, P., Somot, S., Mallet, M., Chiapello, I., Morcrette, J. J., Solmon, F., et al. (2013). A 4-D climatology (1979-2009) of the monthly tropospheric aerosol optical depth distribution over the Mediterranean region from a comparative evaluation and blending of remote sensing and model products. *Atmospheric Measurement Techniques*, *6*(5), 1287–1314. https://doi.org/10.5194/amt-6-1287-2013

North, P. R. J. (2002). Estimation of aerosol opacity and land surface bidirectional reflectance from ATSR-2 dual-angle imagery: Operational method and validation. *Journal of Geophysical Research*, *107*(D12), 4149. https://doi.org/10.1029/2000jd000207

North, P. R. J., Briggs, S. A., Plummer, S. E., & Settle, J. J. (1999). Retrieval of land surface bidirectional reflectance and aerosol opacity from ATSR-2 multiangle imagery. *IEEE Transactions on Geoscience and Remote Sensing*, *37*(1), 526–537. https://doi.org/10.1109/36.739106

Oleson, K. W., Lawrence, D. M., Gordon, B., Flanner, M. G., Kluzek, E., Peter, J., et al. (2010). *Technical Description of Version 4.0 of the community land model (CLM), NCAR/TN-478 + STR* (p. 173). Boulder, CO: National Center for Atmospheric Research. https://doi.org/10.5065/D6FB50WZ

Pozzer, A., De Meij, A., Yoon, J., Tost, H., Georgoulias, A., & Astitha, M. (2015). AOD trends during 2001–2010 from observations and model simulations. *Atmospheric Chemistry and Physics*, *15*(10), 5521–5535. https://doi.org/10.5194/acp-15-5521-2015

Prospero, J. M., Uematsu, M., & Savoie, D. L. (1989). Mineral aerosol transport to the Pacific Ocean. In J. P. Riley (Ed.), *Chemical oceanography* (pp. 187–218). New York, NY: Academic Press.

Putman, W. M., & Lin, S.-J. (2007). Finite-volume transport on various cubed-sphere grids. *Journal of Computational Physics*, *227*(1), 55–78. https://doi.org/10.1016/j.jcp.2007.07.022

Ramanathan, V., Crutzen, P. J., Lelieveld, J., Mitra, A. P., Althausen, D., Anderson, J., et al. (2001). Indian Ocean Experiment: An integrated analysis of the climate forcing and effects of the great Indo-Asian haze. *Journal of Geophysical Research*, *106*(D22), 28371–28398. https://doi.org/10.1029/2001jd900133

Remer, L. A., Kaufman, Y., Tanré, D., Mattoo, S., Chu, D., Martins, J. V., et al. (2005). The MODIS aerosol algorithm, products, and validation. *Journal of the Atmospheric Sciences*, *62*(4), 947–973. https://doi.org/10.1175/JAS3385.1

Remer, L. A., Kleidman, R. G., Levy, R. C., Kaufman, Y. J., Tanré, D., Mattoo, S., et al. (2008). Global aerosol climatology from the MODIS satellite sensors. *Journal of Geophysical Research*, *113*, D14S07. https://doi.org/10.1029/2007JD009661

Sato, Y., Goto, D., Michibata, T., Suzuki, K., Takemura, T., Tomita, H., et al. (2018). Aerosol effects on cloud water amounts were successfully simulated by a global cloud-system resolving model. *Nature Communications*, *9*(1), 985. https://doi.org/10.1038/s41467-018-03379-6

Sayer, A. M., Hsu, N. C., Lee, J., Kim, W. V., Dubovik, O., Dutcher, S., et al. (2018). Validation of SOAR VIIRS over-water aerosol retrievals and context within the global satellite aerosol data record. *Journal of Geophysical Research: Atmospheres*, *123*(23), 13496–13526. https://doi.org/10.1029/2018jd029465

Salomonson, V. V., Barnes, W., Maymon, P. W., Montgomery, H. E., & Ostrow, H. (1989). MODIS: Advanced facility instrument for studies of the Earth as a system. *IEEE Transactions on Geoscience and Remote Sensing*, *27*(2), 145–153. https://doi.org/10.1109/36.20292

Seinfeld, J. H., & Pandis, S. H. (2006). *Atmospheric chemistry and Physics: From air pollution to climate change* (2nd ed.). New York, NY: John Wiley & Sons.

Sheel, V., Guleria, R. P., & Ramachandran, S. (2018). Global and regional evaluation of a global model simulated AODs with AERONET and MODIS observations. *International Journal of Climatology*, *38*, e269–e289. https://doi.org/10.1002/joc.5367

Shrivastava, M., Cappa, C. D., Fan, J., Goldstein, A. H., Guenther, A. B., Jimenez, J. L., et al. (2017). Recent advances in understanding secondary organic aerosol: Implications for global climate forcing. *Reviews of Geophysics*, *55*(2), 509–559. https://doi.org/10.1002/2016rg000540

Smirnov, A., Holben, B., Eck, T., Dubovik, O., & Slutsker, I. (2000). Cloud-screening and quality control algorithms for the AERONET database. *Remote Sensing of Environment*, *73*(3), 337–349. https://doi.org/10.1016/S0034-4257(00)00109-7

Sudo, K., Takahashi, M., Kurokawa, J. i., & Akimoto, H. (2002). Chaser: A global chemical model of the troposphere 1. Model description. *Journal of Geophysical Research*, *107*(D17), ACH 7-1–ACH 7-20. https://doi.org/10.1029/2001jd001113

Takemura, T., Nakajima, T., Dubovik, O., Holben, B. N., & Kinne, S. (2002). Single-scattering albedo and radiative forcing of various aerosol species with a global three-dimensional model. *Journal of Climate*, *15*(4), 333–352. https://doi.org/10.1175/1520-0442(2002)015<0333:Ssaarf>2.0.Co;2

Takemura, T., Nozawa, T., Emori, S., Nakajima, T., & Nakajima, T. (2005). Simulation of climate response to aerosol direct and indirects with aerosol transport-radiation model. *Journal of Geophysical Research*, *110*, D02202. https://doi.org/10.1029/2004JD005029

Takemura, T., Okamoto, H., Maruyama, Y., Numaguti, A., Higurashi, A., & Nakajima, T. (2000). Global three-dimensional simulation of aerosol optical thickness distribution of various origins. *Journal of Geophysical Research*, *105*, 17853–17874. https://doi.org/10.1029/2000JD900265

Takemura, T., Egashira, M., Matsuzawa, K., Ichijo, H., O'ishi, R., & Abe-Ouchi, A. (2009). A simulation of the global distribution and radiative forcing of soil dust aerosols at the Last Glacial Maximum. *Atmospheric Chemistry and Physics*, *9*(9), 3061–3073. https://doi.org/10.5194/acp-9-3061-2009

Taylor, K. E. (2001). Summarizing multiple aspects of model performance in a single diagram. *Journal of Geophysical Research*, *106*(D7), 7183–7192. https://doi.org/10.1029/2000jd900719

Textor, C., Schulz, M., Guibert, S., Kinne, S., Balkanski, Y., Bauer, S., et al. (2006). Analysis and quantification of the diversities of aerosol life cycles within AeroCom. *Atmospheric Chemistry and Physics*, *6*(7), 1777–1813. https://doi.org/10.5194/acp-6-1777-2006

Toth, T. D., Zhang, J. L., Campbell, J. R., Reid, J. S., Shi, Y. X., Johnson, R. S., et al. (2013). Investigating enhanced Aqua MODIS aerosol optical depth retrievals over the mid-to-high latitude Southern Oceans through intercomparison with co-located CALIOP, MAN, and AERONET data sets. *Journal of Geophysical Research: Atmospheres*, *118*(10), 4700–4714. https://doi.org/10.1002/jgrd.50311

Tsigaridis, K., Daskalakis, N., Kanakidou, M., Adams, P. J., Artaxo, P., Bahadur, R., et al. (2014). The AeroCom evaluation and intercomparison of organic aerosol in global models. *Atmospheric Chemistry and Physics*, *14*(19), 10845–10895. https://doi.org/10.5194/acp-14-10845-2014

Twomey, S. (1974). Pollution and the planetary albedo. *Atmospheric Environment*, *8*(12), 1251–1256. https://doi.org/10.1016/0004-6981(74)90004-3

Twomey, S. (1991). Aerosols, clouds and radiation. *Atmospheric Environment. Part A. General Topics*, *25*(11), 2435–2442. https://doi.org/10.1016/0960-1686(91)90159-5

van Marle, M. J. E., Kloster, S., Magi, B. I., Marlon, J. R., Daniau, A. L., Field, R. D., et al. (2017). Historic global biomass burning emissions for CMIP6 (BB4CMIP) based on merging satellite observations with proxies and fire models (1750-2015). *Geoscientific Model Development*, *10*(9), 3329–3357. https://doi.org/10.5194/gmd-10-3329-2017

Wei, J., Peng, Y., Mahmood, R., Sun, L., & Guo, J. (2019). Intercomparison in spatial distributions and temporal trends derived from multi-source satellite aerosol products. *Atmospheric Chemistry and Physics*, *19*(10), 7183–7207. https://doi.org/10.5194/acp-19-7183-2019

Witek, M. L., Garay, M. J., Diner, D. J., Bull, M. A., & Seidel, F. C. (2018). New approach to the retrieval of AOD and its uncertainty from MISR observations over dark water. *Atmospheric Measurement Techniques*, *11*(1), 429–439. https://doi.org/10.5194/amt-11-429-2018

Winker, D. M, Tackett, J. L., Getzewich, B. J., Liu, Z., Vaughan, M. A., & Rogers, R. R. (2013). The global 3-D distribution of tropospheric aerosols as characterized by CALIOP. *Atmospheric Chemistry and Physics*, *13*(6), 3345–3361. https://doi.org/10.5194/acp-13-3345-2013

Wu, G., Hui, L., Yucheng, Z., & Li, W. (1996). A nine-layer atmospheric general circulation model and its performance. *Advances in Atmospheric Sciences*, *13*, 1–18. https://doi.org/10.1007/BF02657024

Xie, Y. Q., Xue, Y., Che, Y. H., Guang, J., Mei, L. L., Voorhis, D., et al. (2017). Ensemble of ESA/AATSR aerosol optical depth products based on the likelihood estimate method with uncertainties. *IEEE Transactions on Geoscience and Remote Sensing*, *56*(2), 997–1007. https://doi.org/10.1109/tgrs.2017.2757910

Xu, K.-M., & Randall, D. A. (1996). A semiempirical cloudiness parameterization for use in climate models. *Journal of the Atmospheric Sciences*, *53*(21), 3084–3102. https://doi.org/10.1175/1520-0469(1996)053<3084:ascpfu>2.0.co;2

Zhang, X. Y., Wang, Y. Q., Niu, T., Zhang, X. C., Gong, S. L., Zhang, Y. M., et al. (2012). Atmospheric aerosol compositions in China: Spatial/temporal variability, chemical signature, regional haze distribution and comparisons with global aerosols. *Atmospheric Chemistry and Physics*, *12*(2), 779–799. https://doi.org/10.5194/acp-12-779-2012

Zhou, L., Bao, Q., Liu, Y., Wu, G., Wang, W.-C., Wang, X., et al. (2015). Global energy and water balance: Characteristics from Finite-volume Atmospheric Model of the IAP/LASG (FAMIL1). *Journal of Advances in Modeling Earth Systems*, *7*(1), 1–20. https://doi.org/10.1002/2014ms000349

Zhou, L., Lin, S.-J., Chen, J.-H., Harris, L. M., Chen, X., & Rees, S. L. (2019). Toward convective-scale prediction within the next generation global prediction system. *Bulletin of the American Meteorological Society*, *100*(7), 1225–1243. https://doi.org/10.1175/bams-d-17-0246.1

Zhou, L., Liu, Y., Bao, Q., Yu, H., & Wu, G. (2012). Computational performance of the high-resolution atmospheric model FAMIL. *Atmospheric and Oceanic Science Letters*, *5*, 355–359. https://doi.org/10.1080/16742834.2012.11447024